REPORT DOCUMENTATION PAGE

AFRL-SR-AR-TR-08-0147

Public reporting burden for this collection of information is estimated to average 1 hour per response, including the time for reviewing gathering and maintaining the data needed, and completing and reviewing the collection of information. Send comments regarding of information, including suggestions for reducing this burden to Washington Headquarters Service, Directorate for Information Op 1215 Jefferson Davis Highway, Suite 1204, Arlington, VA 22202-4302, and to the Office of Management and Budget, Paperwork Reduction Project (0704-0188) Washington, DC 20503.
PLEASE DO NOT RETURN YOUR FORM TO THE ABOVE ADDRESS.

1. REPORT DATE (DD-MM-YYYY)	2. REPORT TYPE Final Technical Report	3. DATES COVERED (From – To) 1 January 2005 – 31 December 2007

4. TITLE AND SUBTITLE
Nonequilibrium Supersonic Magnetogasdynamic Wind Tunnel

5a. CONTRACT NUMBER

5b. GRANT NUMBER
FA9550-05-1-0085

5c. PROGRAM ELEMENT NUMBER

6. AUTHOR(S)
Dr. Igor V. Adamovich

5d. PROJECT NUMBER

5e. TASK NUMBER

5f. WORK UNIT NUMBER

7. PERFORMING ORGANIZATION NAME(S) AND ADDRESS(ES)
The Ohio State University
Department of Mechanical Engineering
Columbus OH   43210

8. PERFORMING ORGANIZATION REPORT NUMBER

9. SPONSORING/MONITORING AGENCY NAME(S) AND ADDRESS(ES)
USAF/AFRL
AFOSR
875 North Randolph Street
Arlington VA 22203
Dr John Schmisseur/NA

10. SPONSOR/MONITOR'S ACRONYM(S)
AFOSR

11. SPONSORING/MONITORING AGENCY REPORT NUMBER
N/A

12. DISTRIBUTION AVAILABILITY STATEMENT

Distribution Statement A: Approved for public release. Distribution is unlimited.

13. SUPPLEMENTARY NOTES

14. ABSTRACT

The report presents results of cold MHD flow deceleration experiments using repetitively pulsed, short pulse duration, high voltage discharge to produce ionization in M=3-4 nitrogen and air flows in the presence of transverse DC electric field and transverse magnetic field. MHD effect on the flow is detected from the flow static pressure measurements. Retarding Lorentz force applied to the flow produces a static pressure increase of up to 20%, while accelerating force of the same magnitude results in static pressure increase of up to 10%. The measured static pressure changes are compared with modeling calculations using quasi-one-dimensional MHD flow equations and with predictions of a 3-D Navier-Stokes / MHD flow code, showing good agreement. Comparison of the experimental results with the modeling calculations shows that the retarding Lorentz force increases the static pressure rise produced by Joule heating of the flow, while the accelerating Lorentz force reduces the pressure rise. The effect is produced for two possible combinations of the magnetic field and transverse current directions producing the same Lorentz force direction (both for accelerating and retarding force).

15. SUBJECT TERMS

16. SECURITY CLASSIFICATION OF:			17. LIMITATION OF ABSTRACT	18. NUMBER OF PAGES	19a. NAME OF RESPONSIBLE PERSON
a. REPORT	b. ABSTRACT	c. THIS PAGE	Unclassified	76	19b. TELEPONE NUMBER (Include area code)

Standard Form 298 (Rev. 8-98)
Prescribed by ANSI-Std Z39-18

NONEQUILIBRIUM SUPERSONIC MAGNETOGASDYNAMIC WIND TUNNEL

(FA9550-05-1-0085)

Final Report

Igor V. Adamovich, Walter R. Lempert, and J. William Rich

Department of Mechanical Engineering
The Ohio State University, Columbus, OH 43210

20080331082

ABSTRACT

The report presents results of cold MHD flow deceleration experiments using repetitively pulsed, short pulse duration, high voltage discharge to produce ionization in M=3-4 nitrogen and air flows in the presence of transverse DC electric field and transverse magnetic field. MHD effect on the flow is detected from the flow static pressure measurements. Retarding Lorentz force applied to the flow produces a static pressure increase of up to 20%, while accelerating force of the same magnitude results in static pressure increase of up to 10%. The measured static pressure changes are compared with modeling calculations using quasi-one-dimensional MHD flow equations and with predictions of a 3-D Navier-Stokes / MHD flow code, showing good agreement. Comparison of the experimental results with the modeling calculations shows that the retarding Lorentz force increases the static pressure rise produced by Joule heating of the flow, while the accelerating Lorentz force reduces the pressure rise. The effect is produced for two possible combinations of the magnetic field and transverse current directions producing the same Lorentz force direction (both for accelerating and retarding force). This demonstrates that the observed static pressure change is indeed due to the MHD interaction, and not due to Joule heating of the flow in the crossed discharge. This result provides first direct evidence of cold supersonic flow deceleration by Lorentz force. Kinetic modeling of the crossed pulser-sustainer discharge in the presence of transverse magnetic field is used to obtain insight into kinetics of a low-temperature MHD nitrogen plasma.

CHAPTER I.

LOW-TEMPERATURE M=3 FLOW DECELERATION BY LORENTZ FORCE

1. Introduction

The use of nonequilibrium (low-temperature) magnetohydrodynamics for supersonic flow control and power generation continues to attract considerable interest. Over the last few years, numerous theoretical system studies and modeling calculations in this field have been complemented by experimental results. In particular, experiments at Ohio State showed that retarding Lorentz force results in significant density fluctuation increase in a supersonic boundary layer in low-temperature M=3 nitrogen and air flows [1,2]. In these experiments, ionization in cold supersonic flows (stagnation temperature T_0=300 K) was generated by transverse RF discharge [1] and by high voltage, short pulse duration, high pulse repetition rate discharge [2]. The repetitively pulsed discharge ionization technique has also been used at Princeton University to demonstrate feasibility of MHD power extraction from a cold M=3 air flow [3]. Finally, nonequilibrium MHD flow experiments at Wright-Patterson AFB showed that a near-surface glow discharge combined with the magnetic field can be used to control surface pressure on a model in a M=5 air flow [4].

Considerable effort has been made to demonstrate cold supersonic flow acceleration or deceleration by Lorentz force, with the main application being MHD flow control in hypersonic inlets [5]. Recent results obtained at Princeton demonstrate Lorentz force acceleration of a constricted discharge filament sustained near the test section wall in a cold M=3 air flow, up to velocities of 1.9 km/sec [6]. If the momentum of the accelerated filament is coupled to the flow due to collisions between the charged species and the neutral species, this would result in the boundary layer flow acceleration (the "snowplow" effect [6]). Indeed, 3-D compressible Navier-Stokes MHD modeling calculations [7] suggest that Lorentz force flow acceleration and deceleration may be detected at the flow conductivities realized at the conditions of our previous experiments [2], both in the boundary layer and in the inviscid core flow. Specifically, for a M=2.6 nitrogen flow at a stagnation pressure of P=1/3 atm, electrical conductivity of σ=0.1 mho/m, magnetic field of B_z=1.5 T, transverse electric field of E_y=±300 V/cm, and the MHD section length of L=5 cm, these calculations predict Mach number change by up to $\Delta M \approx \pm 0.2$. This Mach number change corresponds to a relative static pressure change of $\Delta P/P \approx \pm 30\%$, which

would be easily detectable in the experiment. This suggests that the same experimental apparatus as used in our previous work [2] can be employed to detect the flow acceleration effect.

During the operation of an MHD channel, Joule heat is inevitably generated in addition to the Lorentz force. The ratio of the Joule heat, $j_y E_y$, to the Lorentz force work, $j_y B_z u$, determines the MHD loading parameter, $K = E_y / B_z u$, where $j_y \sim \sigma E_y$ is the transverse current density and u is the flow velocity. Obviously, increasing the electric field at a given conductivity would increase the Lorentz force. However, this would be achieved at the penalty of also increasing the loading parameter, which would mean that a larger fraction of input electrical power would simply heat the gas, without imparting momentum to the flow. In nonequilibrium nitrogen and air plasmas sustained in supersonic flows, the detrimental effect of Joule heating can be significantly reduced due to the well known fact that a major fraction of the electric discharge power at these conditions, up to 98% [8], goes to vibrational excitation of nitrogen. Since the supersonic flow residence time in the MHD section is quite short, $\tau_{res} \sim L/u \sim 0.1$ m / 10^3 m/s ~ 100 μsec, while vibrational relaxation time of nitrogen at low temperature is $P\tau_{VT} \sim 1$ atm·sec [9], vibrational relaxation simply does not have time to occur. In air, vibrational relaxation of nitrogen in the presence of O atoms generated in the discharge is much faster, $P\tau_{VT} \sim 10$ atm·μsec · (n_O/N) [9], where n_O/N is the O atom mole fraction. However, because the O atom fraction in the discharge is rather small, vibrational relaxation would still remain very slow. For this reason, the energy would remain locked in the nitrogen vibrational mode and Joule heating in the discharge would be greatly reduced. The effective MHD loading parameter at these conditions can be defined as follows,

$$K = \frac{\alpha \cdot j_y E_y}{j_y B_z u} = \frac{\alpha \cdot E_y}{B_z u} \quad , \tag{1}$$

where α is the discharge energy fraction going into Joule heating.

This well known effect provided rationale for completely neglecting Joule heating in modeling calculations of Ref. [7], as a first approximation. However, this approach is oversimplified, since it is understood that in the actual low-temperature MHD experiments [2], Joule heating, although significantly reduced, still remained a factor affecting the results. The main objective of the present work is to experimentally study the effect of the Lorentz force on

4

the flow Mach number, determined from static pressure measurements. If the Lorentz force interaction indeed results in significant momentum transfer from the charged species to the entire supersonic flow, the flow static pressure would decrease for both j and B vectors configurations producing an accelerating Lorentz force and increase for the other two configurations producing a retarding Lorentz force. On the other hand, if the electric discharge power at these conditions remains the same, Joule heating would result in a static pressure increase (i.e. Mach number reduction), which would be the same for all four of these cases. In case when both these factors, Lorentz force and Joule heating, generate comparable effects on the flow, the static pressure dependence on the Lorentz force direction should still be apparent.

2. Experimental

The experiments have been conducted at the supersonic nonequilibrium plasma/MHD wind tunnel facility described in greater detail in Refs. [1,2]. Briefly, this facility generates stable and diffuse supersonic nonequilibrium plasmas flow at M=3-4 in a uniform magnetic field up to B=2 T, with run durations from tens of seconds to complete steady state. The schematic of the M=3 supersonic nozzle and an MHD test section is shown in Fig.1. An aerodynamically contoured M=3 supersonic nozzle made of transparent acrylic plastic is connected to a 2 cm x 4 cm rectangular cross section test section 12 cm long with an angle step diffuser. The nozzle / test section / diffuser assembly is attached to a vacuum system connected to a 1200 ft^3 dump tank pumped out by an Allis-Chalmers 1300 cfm rotary vane vacuum pump. The minimum pressure in the vacuum system sustained by the pump is 35-40 torr, which necessitates the use of a supersonic diffuser with the nozzle / test section operated at relatively low stagnation and static pressures (P_0=1/3-1 atm, P_{test}=7-20 torr). The nozzle assembly is equipped with pressure taps measuring plenum pressure as well as static pressures at the beginning and at the end of the test section. The nozzle throat dimensions are 20 mm x 9.5 mm, which gives a mass flow rate through the test section of $\dot{m}$=15 g/sec at P_0=1/3 atm.

Two rectangular electrode blocks 5 cm long are flush mounted in the side test section walls (see Fig. 1). Each electrode block, made of mica ceramic, incorporates a single copper plate electrode 35 mm wide, 45 mm long, and 3 mm thick. The electrode edges are rounded using a Rogowski profile [10] to achieve a more uniform electric field distribution between the electrodes. To accommodate the electrodes, recesses are machined in the ceramic blocks. This

creates a 2 mm thick ceramic layer between each electrode and the flow in the test section. On the opposite sides, the electrodes are covered with 2 mm thick acrylic plates. The gaps between the copper electrodes, the ceramic blocks, and the cover acrylic plates are filled with a self-hardening dielectric compound to preclude electrode surface exposure to air and prevent corona formation near the high-voltage electrode surface. Figure 2 shows a photograph of the M=3 test section. Ionization in the test section is produced using a Chemical Physics Technologies custom designed high-voltage (up to 20-25 kV peak), short pulse duration (~10-20 nsec), high repetition rate (up to 50 kHz) pulsed plasma generator. The plasma generator produces high voltage pulses by compressing 500 V peak, 1 μsec long input pulses using several stages of magnetic compression circuits. The use of the insulated gate bipolar transistor switch allows high pulse repetition rates. During the pulser operation, pulse voltage and current are measured using a Tektronix P6015A high voltage probe and a custom-made low-capacitance resistive current probe.

Transverse DC electrical current (sustainer current) in the supersonic flow ionized by the repetitively pulsed discharge is sustained by applying a DC field (up to 500 V/cm) to two 50 mm x 20 mm DC electrode blocks flush mounted in the top and bottom nozzle walls 4 cm apart, perpendicular both to the flow velocity and to the magnetic field direction, as shown in Fig. 1. The applied DC field, which is far too low to produce additional ionization in the flow, except in the cathode layer, is needed to sustain transverse (MHD) current. The DC electrode blocks are made of boron nitride ceramic, with continuous copper electrodes 45 mm long each. The transverse DC field is applied using a DEL 2 kV / 3A power supply operated in a voltage stabilized mode, with a 0.5-1.0 kΩ ballast. Two inductors 1 mH each were placed in the DC circuit in series with both DC electrodes to attenuate high amplitude current pulse propagation into the DC circuit. Current in the DC sustainer circuit is measured using a Tektronix AM503S current probe.

The entire nozzle / test section / diffuser assembly was placed between the poles of a GMW water cooled electromagnet, as shown in Figs. 1, 2, and attached to a 4 foot long, 6 inch diameter PVC vacuum pipe connected to the vacuum system. To improve the pulsed discharge load impedance matching, the high voltage pulse magnetic compression unit was also mounted inside the magnet, above the test section (see Fig. 2), and short high voltage electrode cables (15 cm long) have been used. The magnet can generate a steady-state magnetic field up to B=3.5 T

between two circular poles up to 25 cm in diameter. In the present experiments, for the distance between the 15 cm diameter poles of 6 cm, the magnetic field at maximum current through the magnet coils of 140 A is B=1.8 T. To preclude external magnetic field penetration into the pulse compression unit, it was placed inside a custom-made six-layer shell magnetic shield made of a high magnetic permeability material with a total wall thickness of 1/2". Multiple layers are necessary because of the magnetic flux saturation in the outermost shield layers in the strong external magnetic field. At the B=1.5 T field between the magnet poles, the field inside the magnetic shield was about 20-30 mT.

Flow temperature downstream of the MHD section was inferred from the nitrogen second positive system emission spectra measured using a Thor Labs 5 m long AFS fiber optic bundle with collimators on each end, and a Princeton Instruments Optical Multichannel Analyzer (OMA) with a 0.5 m monochromator, 1200 g/mm grating blazed at 700 nm, and an ICCD array camera. The collimators were positioned in front of an optical access window in the test section (see Fig. 1), and in front of the slit opening of the spectrometer, respectively. Fiber optic link calibration using a 1.3 mm diameter aperture light source showed the collimator signal collection region to be a cylinder 2-3 mm in diameter and approximately 50 mm long. Therefore these measurements yielded emission spectra averaged along the line of sight passing through the center plane of the flow (see Fig. 1). Rotational temperature of the flow was inferred using a synthetic spectrum with the accurate nitrogen molecular constants [11], rotational like intensities [12], and the experimentally measured slit function of the spectrometer.

In the present experiments, both the magnet and the DC power supply were operated continuously. No breakdown was produced in the test section and no current was measured in the DC circuit until the high voltage pulse train was initiated. After the gas flow was started and test section pressure reached steady state, the pulser was turned on for 0.5-1.0 seconds. After the high voltage pulse train stopped, the discharge always extinguished. Time-dependent static pressure at the end of the test section was monitored by a high accuracy Omega PX811-005GAV pressure transducer, at a sampling rate of 67 Hz (response time of 15 msec). The pressure tap used for these measurements is located in the side wall of the test section, 3 cm downstream of the DC electrodes, as shown in Figs. 1,2. The pressure transducer was placed at a distance of about 2 m from the test section, which was necessary to nearly completely remove electromagnetic interference from the pulsed discharge. Because of the long line between the pressure tap and the

pressure transducer, the actual response time of the transducer may be significantly longer, which required its direct evaluation in the present experiments. As in our previous work [1,2], static pressure was measured for both accelerating and decelerating Lorentz force directions. In both these cases, Lorentz force was generated by two different combinations of the transverse B field and the transverse DC electric field directions. Control runs in a cold supersonic flow without plasmas and in an ionized flow without DC electric field applied, i.e. when the time-averaged Lorentz force is zero, have also been conducted. The purpose of this approach was to isolate the MHD effect, which should depend on the Lorentz force direction, from the polarity-independent effect of Joule heat. The experiments were conducted in nitrogen, dry air, and room air.

3. Results and Discussion

Figure 3 shows typical single pulse voltage and current oscillograms in a M=3 nitrogen flow at P_0=250 torr, P_{test}=8.4 torr, respectively, at the magnetic field of B=1.5 T. The peak voltage and current at these conditions are 13.2 kV and 31.2 A, respectively, with pulse duration (FWHM) of approximately 30 ns. The pulse energy coupled to the flow, calculated from the current and voltage traces at these conditions, was in the range of 1-2 mJ.

Figure 4 shows several voltage pulses generated at the pulse repetition rate of v= 40 kHz, at the same flow conditions. From Fig. 4, it can be seen that at this pulse repetition rate the voltage duty cycle is extremely low, ~30 nsec / 25 μsec ~ 1/1000. The high reduced electric field during the pulses, E/N~$7 \cdot 10^{-15}$ V·cm^2 (70 Td), makes possible efficient ionization by electron impact, the rates of which have strong exponential dependence on E/N [8]. On the other hand, the short pulse duration and the low duty cycle greatly improve the plasma stability. Basically, the pulse duration, ~30 nsec, is much shorter than the characteristic time for the ionization instability development, ~10^{-3}-10^{-4} sec [8].

Figure 5 shows DC sustainer current oscillograms in a pulse-ionized M=3 nitrogen flow at the conditions of Figs. 3 and 4. In Fig. 5, current traces are shown for DC power supply voltage of U_{PS}=2 kV and ballast resistor of R=0.5 kΩ, for two different electric field polarities. Since the DC power supply operates in the voltage stabilized mode, the voltage between the DC electrodes is $U=U_{PS}-IR$, where I is the sustainer current. In this figure, the current pulses produced during the high voltage pulses are not resolved. It can be seen that after each ionizing

pulse the sustainer current reaches approximately I=2 A, with the subsequent fall-off in a decaying plasma between the pulses, to a minimum value of about I=0.5 A. Note that the plasma does not fully decay between the pulses. As can be seen from Fig. 5, the time-averaged currents at these conditions are close, <I>=0.95 and 0.86 A. In dry air at the same flow and plasma conditions, the time average currents were up to <I>=1.0-1.3 A. In the entire range of experimental conditions, the discharge plasma appeared uniform and stable, filling the entire volume of the flow in the MHD section. The magnetic field helped stabilize the discharge, dissipating sustainer current oscillations occurring in the absence of the magnetic field. Photographs of the pulser-sustainer plasmas generated in supersonic flows of nitrogen and air can be found in our recent paper [2]. This behavior suggests that the supersonic plasma flow in the MHD section can be analyzed using a quasi-one-dimensional MHD flow model.

The time-averaged DC discharge power added to the flow at these conditions is approximately 1.1-1.5 kW, which in case of instant thermalization would result in the estimated flow temperature rise of about ΔT=70-100 K, from the baseline core flow temperature at M=2.9 of T=110 K. However, at the reduced electric field in the sustainer discharge of E/N=5-6·10^{-16} V·cm^2 (based on the initial core flow temperature), about 90% of the discharge power in nitrogen and air goes to vibrational excitation of nitrogen [8], vibrational relaxation rate of which is extremely slow [9]. Basically, the slow vibrational relaxation rate locks up the energy stored in nitrogen vibrations and makes the supersonic flow essentially frozen. Assuming that the rest of the discharge power (~10%) thermalizes, the resultant inviscid core flow temperature rise would be significantly lower, only up to ~10 K. Note that energy addition to the flow by the repetitively pulsed discharge, based on the measured single pulse energy, 1-2 mJ, is insignificant, 40-80 W at the pulse repetition rate of ν=40 kHz, or only a few per cent of the energy loading by the DC sustainer discharge.

These estimates are consistent with the flow temperature measurements. Figure 6 shows two $N_2(C^3\Pi_u \rightarrow B^3\Pi_g)$ emission spectra (rotationally unresolved 1→4 band) measured in a M=3 nitrogen flow ionized by a repetitively pulsed discharge at ν=40 kHz and B=1.5 T, (i) without the DC sustainer discharge and (ii) at the highest sustainer discharge power of 1.4 kW, achieved at U_{PS}=2 kV, R=0.5 kΩ, and <I>=0.9 A. Note that these spectra are very nearly identical, although the line-of-sight averaging by the fiber optic collimator includes signal contribution from the boundary layers flowing over the DC electrode surfaces (see Fig. 1), where heating by DC

9

discharge is likely to be most intense. The best fit synthetic spectrum, shown in Fig. 7, indicates the line-of-sight averaged temperature of T=180±20 K for both these cases (i.e. ~40-80 W power added by the pulser alone and ~1.5 kW added by pulser and sustainer together). This temperature is somewhat higher than the isentropic flow temperature at M=2.9, T=110 K. This is most likely due to the line-of sight averaging across the core flow and two boundary layers on the top and bottom walls of the test section (see Fig. 1). Contribution of warm boundary layer regions (with the recovery temperature of $T_r \approx 270$ K) into the emission signal results in raising the "tail" of the vibrational band, thereby increasing the apparent rotational temperature. This effect has also been observed in our previous work on shock wave control in M=2 low-temperature RF plasma flows [13]. We emphasize that the most important result is that the temperatures measured with and without the 1.4 kW DC sustainer discharge turn out to be very close. Note that instant thermalization of the DC sustainer discharge power at these conditions would result to a flow temperature rise of approximately ΔT=90 K. Figure 7, which shows N_2 synthetic spectra at T=100, 180, and 260 K, illustrates the sensitivity of the temperature inference method used, and demonstrates that a temperature rise of 90 K would be easily detected at the present spectral resolution. Therefore, absence of a detectable temperature rise produced by a 1.4 kW DC sustainer discharge is direct evidence of delayed flow thermalization due to slow vibrational relaxation.

Figure 8 shows normalized test section static pressure traces measured in M=3 nitrogen flows at the conditions of Figs. 3-5, with and without Lorentz force applied. The baseline static pressure, measured using the pressure tap downstream of the MHD section shown in Figs. 1, 2, was P=8.4 torr, which corresponds to the Mach number of M=2.9. Turning the pulser on in the presence of magnetic field, without applying transverse DC electric field, i.e. generating ionization in the test section without applying Lorentz force did not produce detectable pressure rise (see Fig. 8). Recent modeling calculations [14,15] suggest that a large fraction of the nanosecond pulsed discharge voltage drops across a thin cathode sheath, which could result in a localized energy deposition and strong near-wall flow heating. Note that if a significant fraction of the pulsed discharge power (~40-80 W) is indeed deposited into a thin cathode sheath, the resultant rapid localized heating would likely produce local pressure increase. However, the results of static pressure measurements with only the pulsed discharge operating, shown in Figs. 8,9, did not show any detectable pressure rise, although the static pressure tap was located on the

10

same wall as the cathode of the pulsed discharge. This suggests that pulsed discharge energy deposition in the cathode sheath is a relatively minor effect at the present experimental conditions.

In addition to this baseline pressure trace, four pressure traces plotted in Fig. 8 correspond to four possible combinations of the transverse current and the magnetic field vector directions, shown schematically in Fig. 1. Two of these combinations result in accelerating Lorenz force, **jxB**, while two others produce retarding Lorentz force. In each one of these runs, the pulser was turned on for 0.5 sec. It can be seen that in all four cases, generating transverse current in the MHD section results in a static pressure increase. This behavior points to Joule heating of the flow by the transverse DC discharge as one of the sources of the pressure rise. However, for both **j** and **B** vector combinations corresponding to the accelerating Lorentz force the pressure rise, 5-7%, is noticeably lower than for both retarding Lorentz force combinations, 18-21%. The dependence of the static pressure rise on the Lorentz force polarity suggests that the pressure and the flow Mach number may also be affected by the MHD force interaction. Similar results were obtained in a dry air flow at the same flow conditions (see Fig. 9), 5-7% for the accelerating Lorentz force and 17-20% for the retarding Lorentz force.

Control runs in nitrogen and dry air have been made with the magnetic field turned off, at B=0. In the absence of the magnetic field, sustainer discharge voltage had to be reduced to $U_{PS}=1$ kV to prevent sustainer current oscillations and instability development. As a result, the discharge power decreased from about 1.5 kW (see Fig. 5) to about 0.5 kW. The sustainer current at these conditions, <I>=0.60-0.65 A, was comparable to the current at B=1.5 T, <I>=0.86-0.95 A (see Fig. 5). In this case, no pressure difference was detected between two DC discharge polarities, the pressure rise being about 3% in both cases (see Fig. 10). This provides additional evidence that the static pressure difference detected at B=1.5 T and shown in Figs. 8,9 is indeed due to the Lorentz force interaction.

To analyze the results of static pressure measurements in the presence of the Lorentz force and Joule heat, we have used quasi-one-dimensional MHD flow equations [16],

$$\frac{dp}{dx} = \frac{1}{M^2 - 1} \cdot \left[-\left\{ (\gamma - 1)M^2 + 1 \right\} \cdot F + \frac{(\gamma - 1)M}{a} \cdot \dot{Q} \right] \qquad (2)$$

11

$$\frac{dM}{dx} = \frac{1}{ap} \cdot \frac{1}{M^2 - 1} \cdot \left\{ u \left(1 + \frac{\gamma - 1}{2} M^2 \right) \cdot F - \frac{\gamma - 1}{2\gamma} \cdot \left(\gamma M^2 + 1 \right) \cdot \dot{Q} \right\} \tag{3}$$

$$\frac{du}{dx} = \frac{u}{p} \cdot \frac{1}{M^2 - 1} \cdot \left(F - \frac{\gamma - 1}{\gamma u} \cdot \dot{Q} \right) \tag{4}$$

$$\frac{dT}{dx} = \frac{T}{p} \cdot \frac{\gamma - 1}{\gamma} \cdot \frac{1}{M^2 - 1} \cdot \left(-\gamma M^2 \cdot F + \frac{\gamma M^2 - 1}{u} \cdot \dot{Q} \right) \quad , \tag{5}$$

where

$$F = j_y B_z \cong \frac{IB}{A} \tag{6}$$

$$\dot{Q} = \alpha \cdot j_y E_y \cong \alpha \cdot \frac{I(U_{PS} - IR)}{Ah} \tag{7}$$

are the Lorentz force and the Joule heat per unit volume, respectively. In Eqs. (6,7), I is the sustainer current, U_{PS} is the DC voltage, R is the ballast resistance, A is the DC electrode surface area, h is the distance between the DC electrodes, and α is the discharge power fraction going to Joule heating (effective Joule heating factor). Note that for small values of the MHD interaction parameter [16],

$$\eta = \frac{\left| j_y B_z \right| L}{\rho u_\infty^2} \quad , \tag{8}$$

the right hand sides of Eqs. (2-5) are nearly constant, and they can be integrated analytically. In Eq. (8), L is the length of the MHD section. Indeed, at the conditions of the present experiments, U_{PS}=2 kV, $I_y \approx 1.0$ A, R=0.5 kΩ, B=1.5 T, A=9 cm^2, L=4.5 cm, $\rho \approx 0.03$ kg/m^3, and $u_\infty \approx 600$ m/sec,

12

the interaction parameter is quite low, $\eta \approx 7 \cdot 10^{-3}$. Then integrating Eq. (2) gives the following expressions for the pressure rise difference between the retarding and the accelerating Lorentz force cases, $\Delta p_R - \Delta p_A$,

$$\Delta p_R - \Delta p_A \cong 2 \cdot \frac{(\gamma - 1)M^2 + 1}{M^2 - 1} \cdot j_y B_z L \tag{9}$$

and for the effective Joule heating factor,

$$\alpha \cong \frac{\Delta p_A + \Delta p_R}{2} \frac{M^2 - 1}{(\gamma - 1)M} \frac{a}{j_y E_y L} \tag{10}$$

For the baseline conditions, p=8.5 torr, T=110 K, M=2.9, γ=1.4, Eq. (9) gives $(\Delta p_R - \Delta p_A)/p \approx 0.08$ for I=1 A. Note that the estimated pressure difference is consistent with the experimental results for nitrogen and air shown in Figs. 8,9. Using Eq. (10) with the results of Fig. 8, the effective Joule heating factor is $\alpha \approx 0.11 \pm 0.02$. The effective Joule heating factor inferred from the static pressure rise measurements is in good agreement with the results of Bolzmann equation solution [17], α=0.09 in nitrogen at the reduced electric field of E/N=6·10^{-16} V·cm^2 and α=0.10 in air at E/N=5·10^{-16} V·cm^2. At these conditions, the effective MHD loading parameter (the ratio of the Joule heating and the Lorentz force work), given by Eq. (1), is K≈4. Therefore, this analysis suggests that the observed static pressure difference between the accelerating and the retarding Lorentz force runs is indeed due to the MHD force interaction, superimposed on the pressure rise due to Joule heating of the flow in the discharge.

The rate of the flow velocity change due to MHD interaction, predicted by Eq. (4), can be also estimated from simple analysis of momentum transfer from the charged particles (electrons and ions) to the neutrals by collisions. Indeed, the Lorentz force applied to the plasma as a whole is balanced by the collision drag force,

$$e(n_e \mu_e + n_i \mu_i) E_y B_z = (n_e m_e \nu_{en} + n_i m_i \nu_{in})(u_p - u) \tag{11}$$

13

Note that the Coulomb forces on the electrons and the ions produced by the Hall (polarization) field cancel out. In Eq. (11), n_e and n_i are electron and ion number densities, respectively, m_e and m_i are their masses, μ_e and μ_i are their mobilities, v_{en} and v_{in} are electron-neitral and ion-neutral collision frequencies, and u_p-u is the plasma velocity relative to the flow (ion slip velocity [18]). Assuming that charge separation in the plasma due to the Hall effect is small, so that $n_e \approx n_i$, and using $\mu_e = e/m_e v_{en}$ and $\mu_i = e/m_i v_{in}$, we have

$$e(\mu_e + \mu_i)E_y B_z = \left(\frac{1}{\mu_e} + \frac{1}{\mu_i}\right)(u_p - u) \tag{12}$$

Finally, remembering that $\mu_e \gg \mu_i$, the ion slip velocity is

$$u_p - u \approx \mu_e \mu_i E_y B_z \tag{13}$$

Equation (13), obtained in Ref. [19] using a more detailed and rigorous analysis, is in good agreement with recent measurements of the ion slip velocity (near-surface constricted discharge filament velocity) in a weakly ionized low-temperature M=3 flow at B=2 T [6]. Since the neutral velocity changes in an ion-neutral collision and in a electron-neutral collision are ~(u_p-u) and ~$(m_e/m_i)(u_p-u) \ll (u_p-u)$, respectively, the net rate of the neutral flow velocity change is

$$\frac{du}{dt} \approx v_{in} \frac{n_e}{N}(u_p - u) = \frac{j_y B_z}{\rho} = \frac{F}{\rho} \tag{14}$$

Finally, remembering that $\rho = \gamma p M^2/u^2$, we obtain

$$\frac{du}{dx} \approx \frac{u}{P} \frac{F}{\gamma M^2} \tag{15}$$

14

which at $M^2 \gg 1$ and in the absence of Joule heat is consistent with Eq. (4). This simple estimate, along with the ion slip velocity measurements [6], demonstrates that phenomenological MHD flow equations, Eqs. (2-5), are consistent with the plasma behavior on the microscopic level.

To estimate the effect of the rate of vibrational relaxation of nitrogen on the effective Joule heating factor, α, one series of experiments was done in room air. In this case, two additional factors change the sustainer discharge characteristics considerably. First, energy added to the vibrational mode of nitrogen by the sustainer discharge thermalizes more rapidly due to fast vibrational relaxation of nitrogen on water vapor, $P\tau_{VT} \sim 10$ atm·μsec at room temperature [20]. Second, electrons in the plasma rapidly attach to oxygen in three-body collisions with water molecules,

$$e + O_2 + H_2O \rightarrow O_2^- + H_2O \quad , \qquad (16)$$

with a near gas kinetic rate, $k = 1.4 \cdot 10^{-29}$ cm^6/s [8]. The latter effect is clearly evident in Fig. 11, which shows sustainer discharge currents in M=3 dry air and room air flows at the same conditions, P_0=250 torr, P_{test}=8.7 torr, B=1.5 T, U_{PS}=2 kV, and R=1.0 kΩ. It can be seen that adding water vapor reduces the current decay time (plasma life time) by about an order of magnitude, from about 25 μsec to about 2-3 μsec. Because of this, the time-averaged current in Fig. 11 also drops by a factor of ten, from <I>=0.51 A to <I>=0.052 A, which suggests that the Lorentz force effect in room air flows would be negligibly small. Indeed, Fig. 12 shows essentially no difference in static pressures rise for the accelerating and retarding Lorentz force directions in room air flows at these conditions. However, from Fig. 12 it can be seen that the static pressure rise due to Joule heating in room air, 6±2%, is comparable to the pressure rise in dry air at the same flow conditions (see Fig. 9), in spite of an order of magnitude difference in the sustainer discharge current and power. Using Eq. (10) with the results of Fig. 12 gives an estimate of the effective Joule heating factor in room air, α=0.4±0.15. This result shows that adding water vapor substantially accelerates the rate of Joule heating in supersonic nonequilibrium plasma flows, most likely due to accelerated vibrational relaxation of nitrogen.

The characteristic time for the flow static pressure change due to both MHD forcing and Joule heating of the supersonic core flow should be comparable with the flow residence time in the discharge section, ~100 μsec. However, the pressure rise/fall time measured in the present

15

experiments is much longer, ~0.2 sec (see Figs. 8-10, 12), which is about an order of magnitude longer than the time resolution of the data acquisition system used, about 15 msec. Clearly, the measured rise/fall time is affected by an additional factor. Varying the length of the ¼" diameter plastic line connecting the wall static pressure tap and the pressure transducer showed that it is in fact the long line that controls the pressure measurement system response time. Indeed, Fig. 13 shows the normalized static pressure signals measured at the same conditions, in a M=3 nitrogen flow with a retarding Lorentz force applied, for two different line lengths, 1.9 m and 4.4 m. It can be seen that increasing the line length also increased the signal response time from about 0.2 sec to about 0.5 sec, without changing the steady-state pressure value. In the present experiments, removing the line and placing the pressure transducer near the static pressure tap was not feasible because of strong electromagnetic interference of the pulsed discharge with the transducer.

Figure 14 compares static pressure measurements with the results of numerical integration of Eqs. (2-5), for three different values of the effective Joule heating parameter, $\alpha=0$ (no Joule heating), $\alpha=0.05$, and $\alpha=0.10$. Experimental points in Fig. 14 are obtained by measuring the static pressure 0.2 seconds after turning the pulser on, approximately at the moment when the pressure reached near steady state. In Fig. 14, positive values of the current correspond to the accelerating Lorentz force. It can be seen that the results of calculations for $\alpha=0.10$ are in good agreement with the experimental data. Figure 14 also illustrates how Joule heating superimposed over Lorentz force affects the static pressure change. Specifically, while the calculations at $\alpha=0$ (no Joule heating) predict static pressure reduction (i.e. Mach number increase) for the accelerating MHD force and static pressure increase (i.e. Mach number reduction) for the retarding MHD force, Joule heating results in static pressure rise in both cases. However, the predicted static pressure increase is always higher for the retarding MHD force, which was observed in the present experiments.

Figure 15 plots the calculated flow Mach number at the conditions of Fig. 14. Comparing the results shown in Fig. 14 and Fig. 15 at $\alpha=0.10$, it can be seen that at I=1.0 A flipping the Lorentz force direction from accelerating to retarding results in a Mach number change from M=2.77 to 2.64 ($\Delta M=-0.13$). Since the baseline Mach number is M=2.89, it is apparent that in both these cases the combined effect of Lorentz force and Joule heating results in flow deceleration. However, as expected, flow deceleration is more pronounced for the retarding

16

Lorentz force. From Fig. 15, one can also see that in the absence of Joule heating the Mach number change at I=1.0 A would be from M=2.96 to M=2.83 (at the same baseline Mach number of M=2.89), ΔM=-0.13. This Mach number change is lower than predicted by the 3-D compressible MHD Navier-Stokes calculations [7], ΔM=-0.4 at the baseline Mach number of M=2.6. However, in these calculations the MHD current was assumed to be I=3 A, which is approximately a factor of three higher than has been achieved in the present experiments. Raising transverse current in the quasi-one-dimensional model of Eqs. (2-5) up to I=3 A results in the increase of the Mach number change, ΔM=-0.42, which is very close to the result obtained in Ref. [7].

Figure 16 summarizes the results for the normalized static pressure difference for two Lorentz force directions, $(\Delta p_R - \Delta p_A)/p$, as a function of the transverse sustainer current obtained in M=3 nitrogen and dry air flows. It can be seen that the measured relative pressure change increases nearly proportional to the current and reaches about 13% at <I>=1.2-1.3 A. This behavior is in good agreement with the quasi-1-D MHD theory, both an approximate analytic solution, Eq. (9), and numerical integration of coupled Eqs. (2-5).

We conclude that the dependence of the static pressure change on the Lorentz force magnitude and polarity, which is consistent with the results of the quasi-one-dimensional MHD flow analysis, conclusively demonstrates supersonic flow deceleration by the Lorentz force. We emphasize that this effect could be detected only because the Joule heating factor in nitrogen and in dry air is small, α=0.1. If this were not the case, at low electrical conductivities achieved at the present experimental conditions the MHD effect would be overshadowed by Joule heating of the flow. To the best of our knowledge, this is the first time this effect was experimentally demonstrated in cold supersonic gas flows. This result, however, does not show feasibility of large-scale MHD deceleration of supersonic flows, discussed in Ref. [6]. This would require analysis of other critical technical issues, such as sustaining magnetic field and low energy cost external ionization over large volumes of the flow, as well as boundary layer separation in a decelerating flow.

Demonstration of net MHD acceleration of the flow, when the Mach number increase and the static pressure is reduced, would require reducing Joule heating, $\dot{Q}$, while keeping the Lorentz force, F, the same. From Eqs. (2,3), it can be seen that this is equivalent to reducing the loading parameter, determined by Eq. (1), to K~1. Since at the present experimental conditions

17

the loading parameter is K~4 (at $\alpha=0.1$), this suggests that net flow acceleration could be achieved if either the effective Joule heating factor or transverse electric field are reduced by a factor of four, down to $\alpha=0.025$ or $E_y=100$ V/cm, respectively, or if the magnetic field is increased by a factor of four, up to B=6 T. Note that keeping the Lorentz force the same while reducing the electric field can be done only if the effective electrical conductivity of the flow, σ, is increased, so that the same transverse current, $j_y \sim \sigma E_y$, would be sustained at a lower transverse electric field. Therefore reducing the electric field by a factor of four would require quadrupling the conductivity.

Although the Mach number change inferred from the present static pressure measurements is consistent with the predictions of the three-dimensional compressible MHD Navier-Stokes calculations [7], these calculations were conducted neglecting Joule heating of the flow in the discharge and forces on the plasma (including ion slip). More accurate modeling calculations, taking into account dynamics of the plasma and the experimentally evaluated discharge energy fraction going into Joule heating, would provide better insight into MHD acceleration and Joule heating of both inviscid core flow and boundary layers.

4. Summary

The paper presents results of cold MHD flow deceleration experiments using repetitively pulsed, short pulse duration, high voltage discharge to produce ionization in M=3 nitrogen and air flows in the presence of transverse DC electric field and transverse magnetic field. MHD effect on the flow is detected from the flow static pressure measurements. Retarding Lorentz force applied to the flow produces a static pressure increase of up to 17-20%, while accelerating force of the same magnitude applied to the same flow results in static pressure increase of up to 5-7%. The effect is produced for two possible combinations of the magnetic field and transverse current directions producing the same Lorentz force direction (both for accelerating and retarding force). This demonstrates that the observed static pressure change is indeed due to the MHD interaction, and not due to Joule heating of the flow in the crossed discharge. No discharge polarity effect on the static pressure was detected in the absence of the magnetic field. The measured static pressure changes are compared with modeling calculations using quasi-one-dimensional MHD flow equations. The fraction of the discharge input power going into Joule heat in nitrogen and dry air, $\alpha=0.1$, has been inferred from the present experiments, and used as

one of the input parameters in the MHD flow model. This fraction is low, primarily because most of the discharge power remains frozen in the vibrational energy mode of nitrogen, and increases to $\alpha=0.4\pm0.15$ in room air because of rapid nitrogen relaxation on water vapor. Comparison of the experimental results with the modeling calculations shows that the retarding Lorentz force increases the static pressure rise produced by Joule heating of the flow in the discharge, while the accelerating Lorentz force reduces the pressure rise. This result provides first direct evidence of cold supersonic flow deceleration by Lorentz force.

References

1. R. Meyer, M. Nishihara, A. Hicks, N. Chintala, M. Cundy, W.R. Lempert, I.V. Adamovich, and S. Gogineni, "Measurements of Flow Conductivity and Density Fluctuations in Supersonic Nonequilibrium MHD Flows", AIAA Journal, vol. 43, No. 9, 2005, pp. 1923-1930

2. M. Nishihara, N. Jiang, J.W. Rich, W.R. Lempert, I.V. Adamovich, and S. Gogineni, "Low-Temperature Supersonic Boundary Layer Control Using Repetitively Pulsed MHD Forcing", Physics of Fluids, 2005, vol. 17, No. 10, pp. 106102-106102-12

3. R.C. Murray, S.H. Zaidi, M.R. Carraro, L.M. Vasilyak, S.O. Macheret, M.N. Shneider, and R.B. Miles, "Magnetohydrodynamic Power Generation Using Externally Ionized, Cold, Supersonic Air as Working Fluid", AIAA Journal, vol. 44, No. 1, 2006, pp. 119-127

4. J. S. Shang, R. Kimmel, J. Hayes, C. Tyler and J. Menart, "Hypersonic Experimental Facility for Magnetoaerodynamic Interactions", Journal of Spacecraft and Rockets, vol. 42, No. 5, 2005, pp. 780-789

5. A.L. Kuranov and E.G. Sheikin, "Magnetohydrodynamic Control on Hypersonic Aircraft under "Ajax" Concept", Journal of Spacecraft and Rockets, vol. 40, No. 2, 2003, pp. 174-182

6. S. Zaidi, T. Smith, S. Macheret, and R. Miles, "Snowplow Surface Discharge in Magnetic Field for High Speed Boundary Layer Control", AIAA Paper 2006-1006, 44nd AIAA Aerospace Sciences Meeting and Exhibit, Reno, Nevada, Jan. 9-12, 2006

7. P. Rawat, X. Zhong, V. Singh, and S. Gogineni, "Numerical Simulation of Secondary Flow in a Weakly Ionized Supersonic Flow with Applied Electromagnetic Field", AIAA Paper

2005-5050, 36th AIAA Plasmadynamics and Lasers Conference, Toronto, Ontario, June 6-9, 2005

8. Yu. P. Raizer, "Gas Discharge Physics", Springer-Verlag, Berlin, 1991

9. B. F. Gordiets, V. A. Osipov, and L. A. Shelepin, Kinetic Processes in Gases and Molecular Lasers, Gordon and Breach, London, 1988

10. J. D. Cobine, "Gaseous Conductors: Theory and Engineering Applications", Dover Publications, New York, 1958

11. F. Roux, F. Michaud, and M. Vervloet, "High Resolution Fourier Spectrometry of $^{14}N_2$ Violet Emission Spectrum: Extensive Analysis of the $C3\Pi_u$-$B^3\Pi_g$ System", Journal of Molecular Spectroscopy, vol. 158, 1993, pp. 270-277

12. A. Budo, " Intensitatsformeln fur die Triplettbanden", Zeitschrift fur Physik, Vol. 105, 1937, pp. 570-587

13. S. Merriman, E. Plönjes, P. Palm, and I.V. Adamovich "Shock Wave Control by Nonequilibrium Plasmas in Cold Supersonic Gas Flows", AIAA Journal, vol. 39, No. 8, 2001, pp. 1547-1552

14. S.O. Macheret, M.N. Shneider, and R.B. Miles, "Modeling of Air Plasma Generation by Repetitive High-Voltage Nanosecond Pulses," IEEE Transactions on Plasma Science, Vol. 30, No. 3, 2002, pp. 1301-1314

15. S.O. Macheret, M.N. Shneider, and R.C. Murray, "Ionization in Strong Electric Fields and Dynamics of Nanosecond-Pulse Plasmas", Physics of Plasmas, Vol. 13, 023502-023502-10, 2006

16. G. W. Sutton and A. Sherman, "Engineering Magnetohydrodynamics", McGraw-Hill, New York, 1965

17. I. V. Adamovich, J. W. Rich, and G. L. Nelson, "Feasibility Study of Magneto-hydrodynamics Acceleration of Unseeded and Seeded Air Flows," AIAA Journal, vol. 36, 1990, p. 590

18. R. J. Rosa, "Magnetohydrodynamic Energy Conversion", McGraw-Hill, 1968

19. S.O. Macheret, "Physics of Magnetically Accelerated Nonequilibrium Surface Discharges in High-Speed Flow", AIAA Paper 2006-1005, 44nd AIAA Aerospace Sciences Meeting and Exhibit, Reno, Nevada, Jan. 9-12, 2006

20. H.E. Bass, S.D. Hoffman, H.-J. Bauer, "Laser Induced Fluorescence Study of the Deactivation of N_2^* by H_2O, H_2S, and CH_4", J. Chem. Phys., vol. 72, No. 3, 1980, pp. 2113-2119
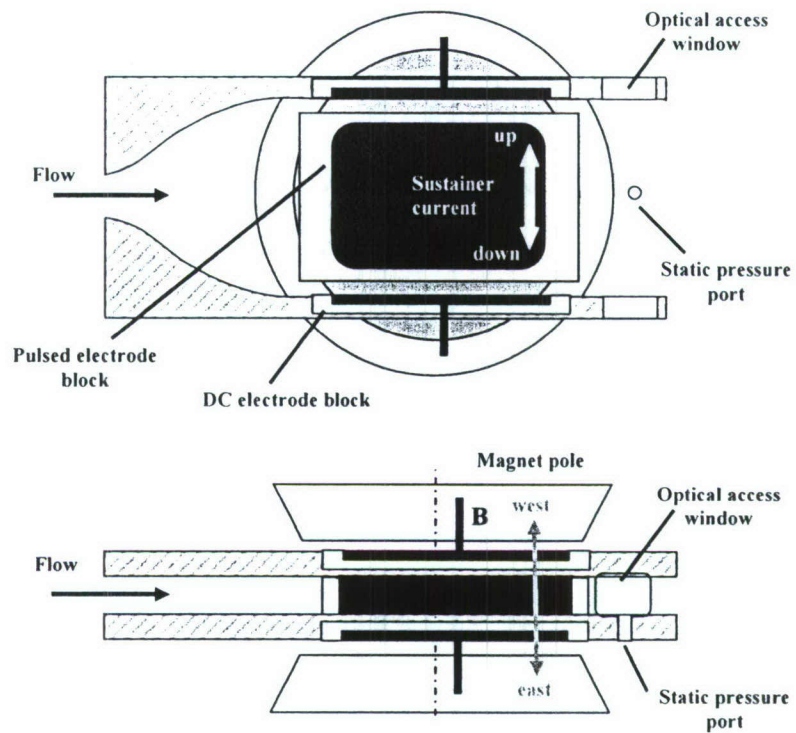
Figure 1. Schematic of a supersonic nozzle and MHD test section
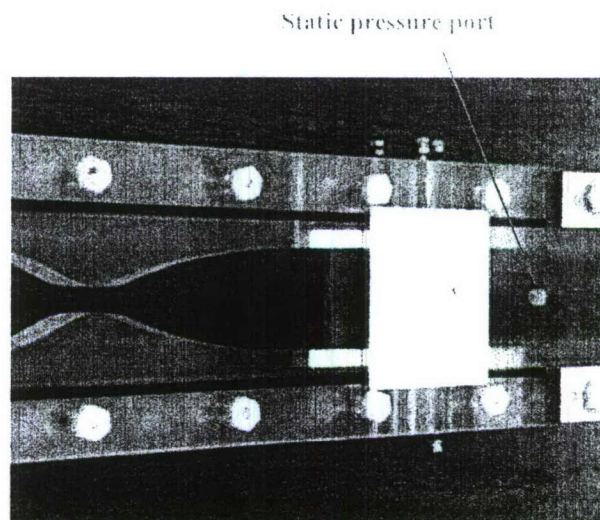
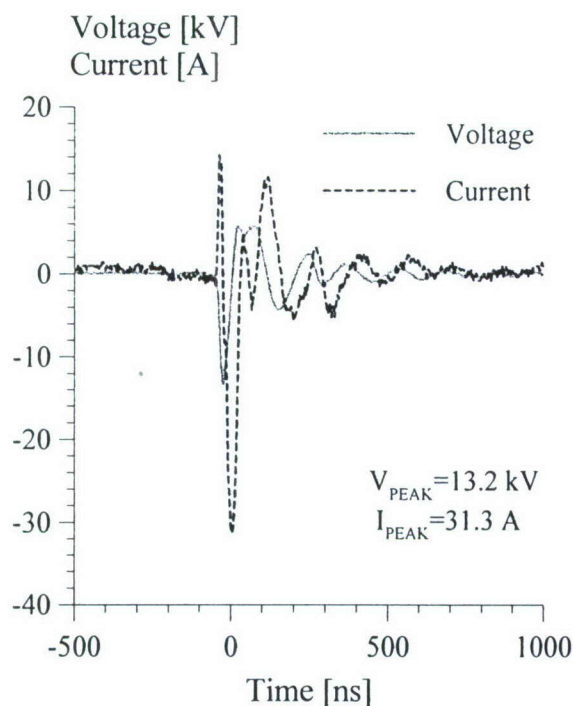**Figure 2.** Photograph of a M=3 test section

Figure 3. Single-pulse voltage and current oscillograms in a M=3 nitrogen flow at P_0=250 torr, P_{test}=8.4 torr, and B=1.5 T.
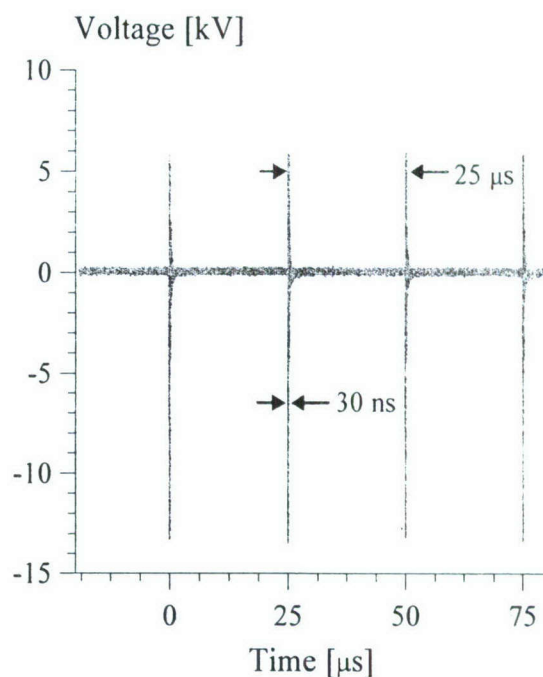

Figure 4. Repetitively pulsed voltage oscillogram in a M=3 nitrogen flow at P_0=250 torr, P_{test}=8.4 torr, and B=1.5 T. Pulse repetition rate is ν=40 kHz.
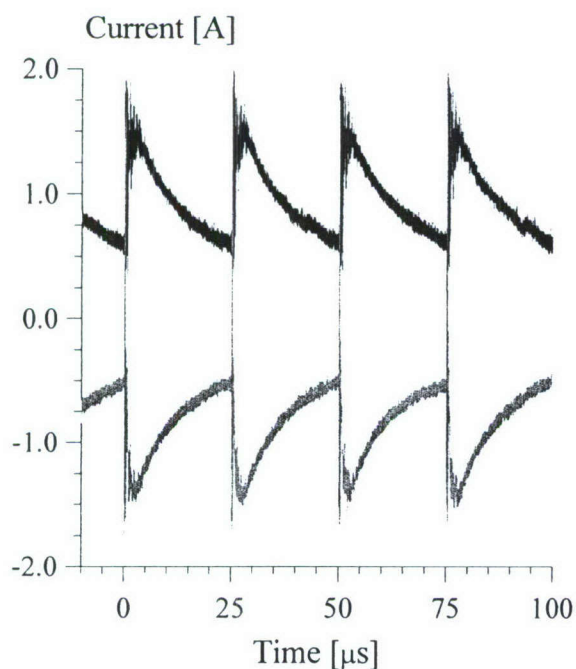
Figure 5. Sustainer (Faraday) current traces for two different transverse DC electric field polarities, at the conditions of Fig. 4. U_{PS}=2 kV, R=0.5 kΩ. Time-averaged currents are 0.95 A (top curve) and 0.86 A (bottom curve).
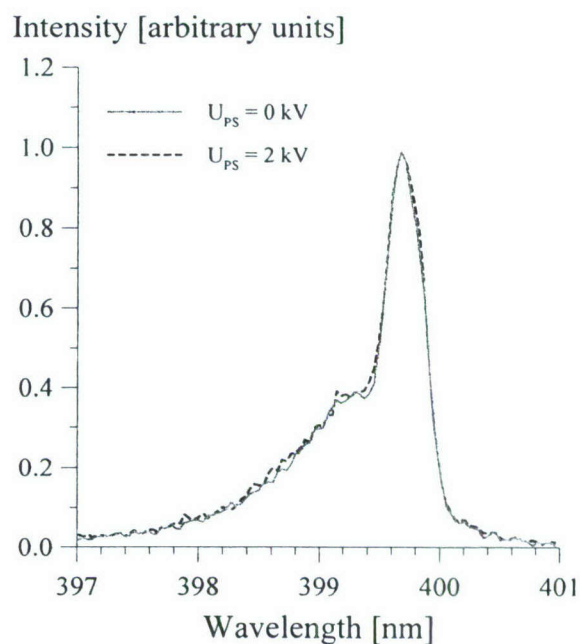
Figure 6. $N_2(C3\Pi_u \rightarrow B^3\Pi_g)$ emission spectra (1→4 band) in a M=3 nitrogen flow at P_0=250 torr, B=1.5 T, and ν=40 kHz, with and without 1.4 kW DC sustainer discharge. Synthetic spectrum fit indicates rotational temperature of T=180±20 K in both cases.

Intensity [arbitrary units]
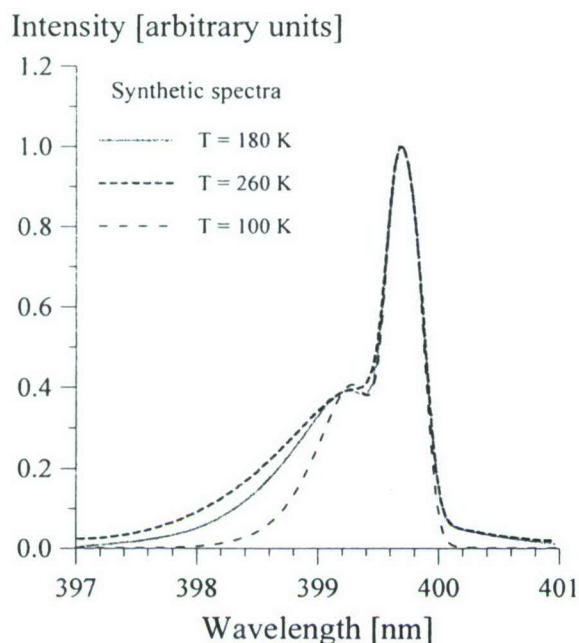
Figure 7. $N_2(C3\Pi_u \rightarrow B^3\Pi_g)$ synthetic spectra (1→4 band) at T=100, 180, and 160 K, illustrating the temperature inference method sensitivity.
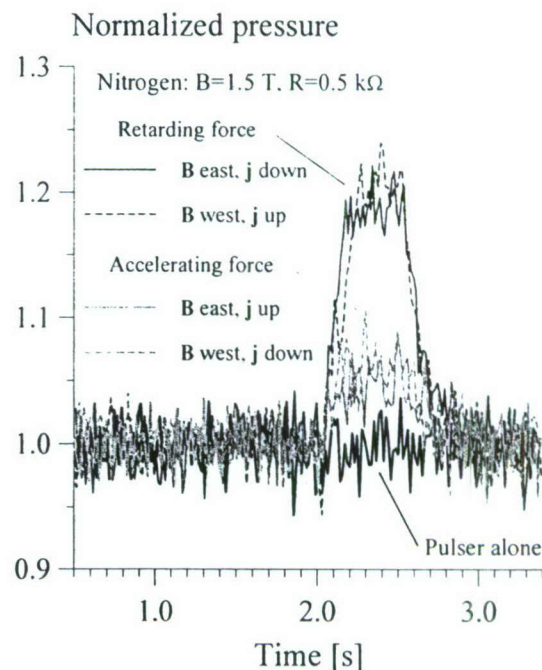
Figure 8. Normalized static pressure traces at the conditions of Figs. 3-5. Lorentz force is applied for 0.5 sec duration. Two pressure traces corresponding to two combinations of current (**j**) and magnetic field (**B**) vectors are shown for both accelerating and retarding force directions.
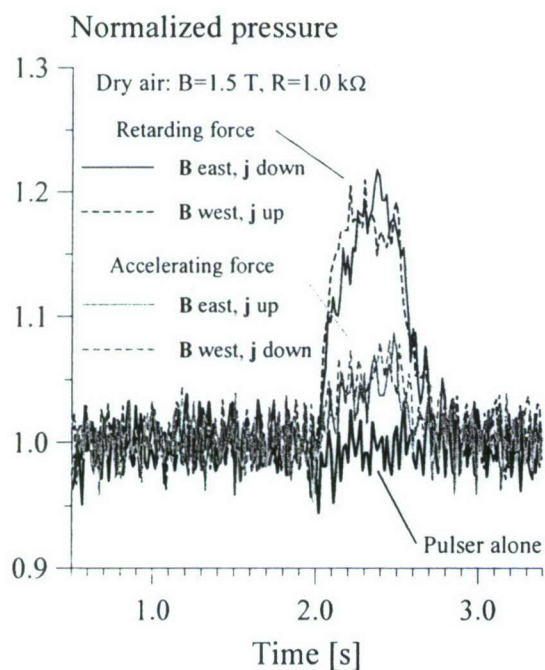

Figure 9. Normalized static pressure traces in M=3 dry air flows at P_0=250 torr, P_{test}=8.7 torr, B=1.5 T, ν=40 kHz. U_{PS}=2 kV, R=1.0 kΩ. Lorentz force is applied for 0.5 sec duration. The legend is the same as in Fig. 6.
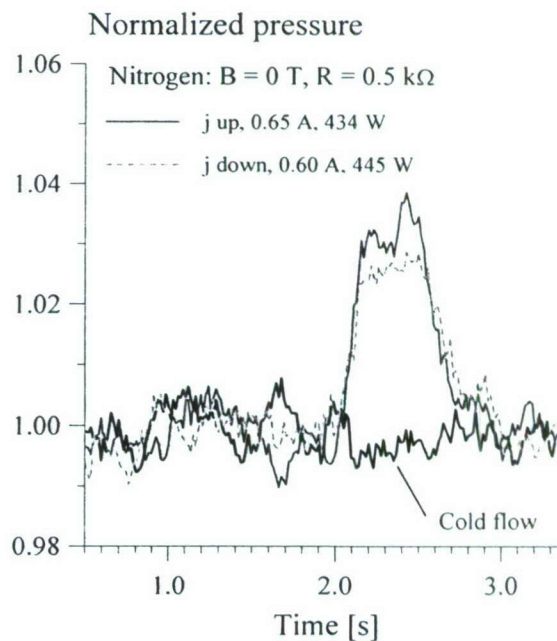
Figure 10. Normalized static pressure traces in M=3 nitrogen flows at P_0=250 torr. U_{PS}=1 kV, R=0.5 kΩ, without magnetic field. Two pressure traces corresponding to two different transverse DC electric field polarities are shown.

24
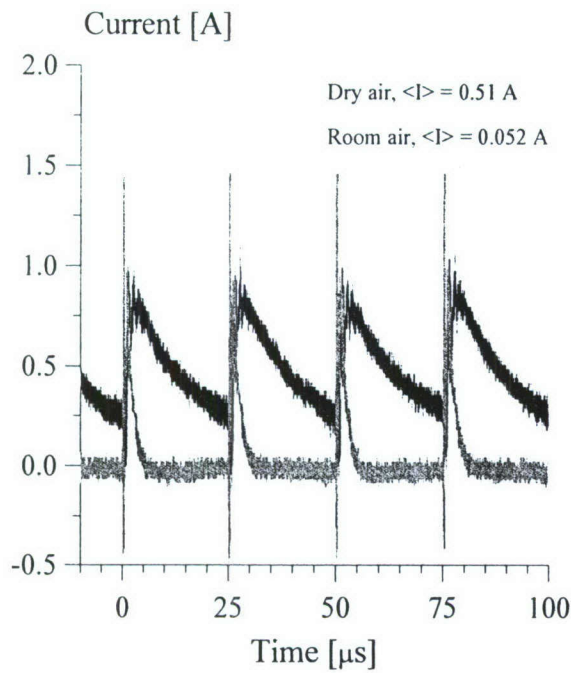
Figure 11. Sustainer (Faraday) current traces in dry air and in room air, at the conditions of Fig. 7. U_{PS}=2 kV, R=1.0 kΩ. Time-averaged currents are 0.51 A (dry air, top curve) and 0.052 A (room air, bottom curve).
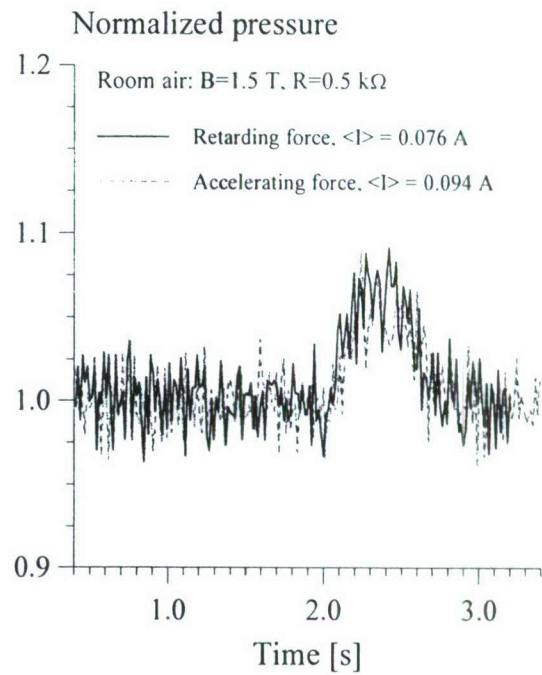

Figure 12. Normalized static pressure traces in M=3 room air flows at the conditions of Fig. 8. Lorentz force is applied for 0.5 sec duration.
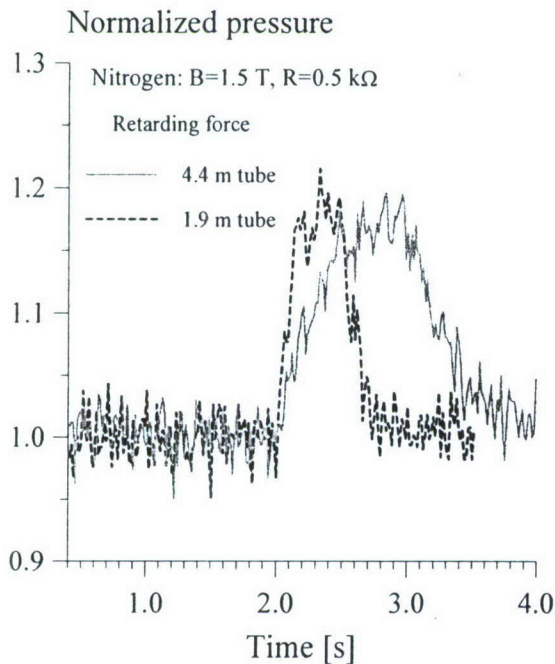

Figure 13. Effect of the pressure tap line length on the measured static pressure rise/fall time. Retarding Lorentz force is applied for 0.5 sec duration. Nitrogen flow conditions are the same as in Figs. 4, 6.
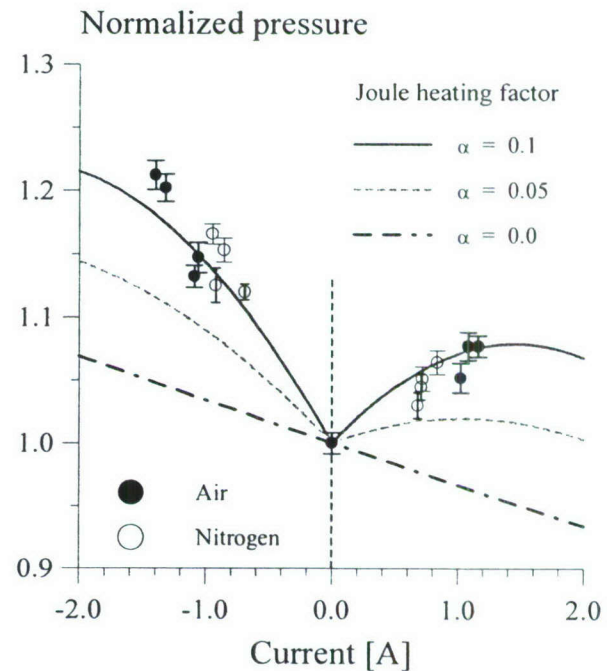

Figure 14. Experimental and calculated normalized pressure in nitrogen and air at P_0=250 torr, U_{PS}=1 kV, and R=0.5 kΩ Calculation results are shown for different values of the Joule heating factor, α.
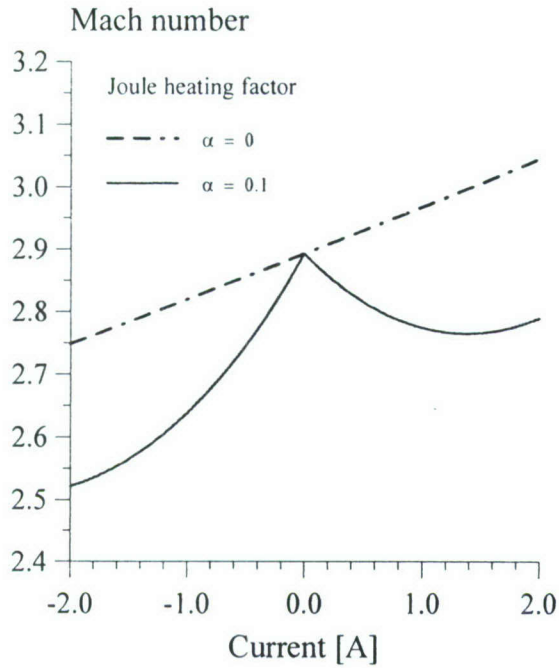
25

Mach number

Figure 15. Calculated Mach number change in nitrogen and air at P_0=250 torr, for α=0.1. At I=±1 A, the Mach number change is 0.13 (from M=2.64 to M=2.77).

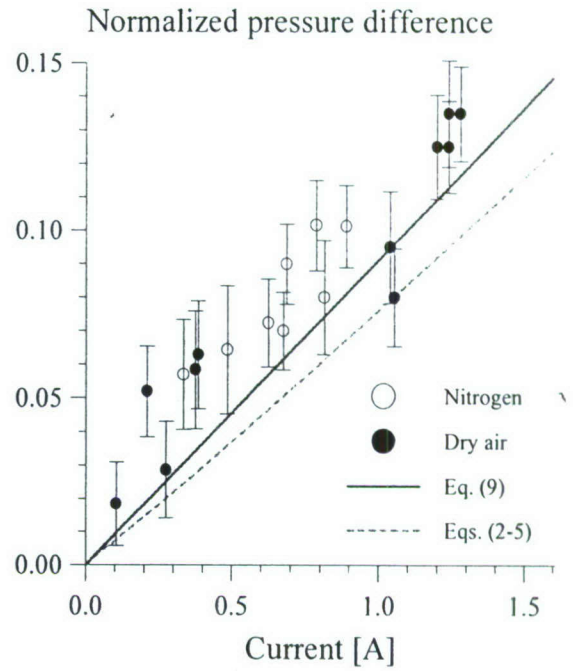## Normalized pressure difference

Figure 16. Experimental and calculated normalized pressure difference, $(\Delta p_R - \Delta p_A)/p$, as a function of the MHD current.

CHAPTER II.

EXPERIMENTAL AND COMPUTATIONAL STUDIES OF LOW-TEMPERATURE M=4 FLOW DECELERATION BY LORENTZ FORCE

1. Introduction

Recent experimental studies of low-temperature MHD flows using ionization produced in the flow by repetitively pulsed nonequilibrium plasmas demonstrated feasibility of MHD high-speed air flow control. In particular, these experiments showed that a retarding Lorentz force results in a density fluctuation increase in a supersonic boundary layer in low-temperature M=3 nitrogen and air flows [1]. MHD power extraction was demonstrated in a cold M=3 air flow [2]. Finally, low-temperature M=3 air flow deceleration by the Lorentz force was detected from the static pressure measurements [3]. In these experiments, ionization in cold supersonic flows (stagnation temperature T_0=300 K) was generated by a high voltage, short pulse duration, high pulse repetition rate discharge, and Faraday current was sustained by transverse DC electric field.

The flow deceleration results of Ref. [3] are consistent with 3-D compressible Navier-Stokes MHD modeling calculations [4], which suggest that Lorentz force flow acceleration and deceleration may indeed be detected at the flow conductivities realized at the conditions of experiments [1,3]. Specifically, for a M=2.6 nitrogen flow at a stagnation pressure of P=1/3 atm, electrical conductivity of σ=0.1 mho/m, magnetic field of B_z=1.5 T, transverse electric field of E_y=±300 V/cm, and the MHD section length of L=5 cm, these calculations predict Mach number change by up to $\Delta M \approx$ ±0.2. This Mach number change corresponds to a relative static pressure change of $\Delta P/\approx$ ±0.3, which would be easily detectable in the experiment. Note that in the modeling calculations of Ref. [4], Joule heating of the flow by the discharge was completely neglected, since it is well known that in nonequilibrium nitrogen and air plasmas, direct Joule heating is significantly reduced because a major fraction of the electric discharge power, up to ~98% [8], goes to vibrational excitation of nitrogen. Indeed, effective Joule heating factor, α (i.e. the discharge energy fraction going into Joule heating of the flow), measured in our previous experiments [3] is rather low, α~0.1. However, we believe that this approach is oversimplified, since it is understood that in the actual low-temperature MHD experiments [2], Joule heating, although significantly reduced, still remains an important factor affecting the results.

The main objective of the present work is to study the effect of the Lorentz force on the flow Mach number, determined from static pressure measurements, and to predict this effect using a 3-D compressible Navier-Stokes / MHD flow modeling code. This work follows up our previous experiments [3] in M=3 nitrogen and air flows. However, a new design of the supersonic test section used in the present work helps improving the flow quality and reducing the boundary layer thickness in the test section. Also, the present experiments are conducted in a M=4 flow, using a higher power plasma pulse generator producing a higher flow conductivity. Finally, the results of present experiments and modeling calculations will be used to determine whether the MHD flow deceleration effect can be detected by a non-intrusive optical diagnostics technique, Molecular Tagging Velocimetry.

2. Experimental

The experiments have been conducted at the supersonic nonequilibrium plasma/MHD blowdown wind tunnel facility described in greater detail in Refs. [1,3]. Briefly, this facility generates stable and diffuse supersonic nonequilibrium plasmas flows at M=3-4 in a uniform magnetic field up to B=2 T. Figure 1 shows photographs of a supersonic nozzle / MHD test section / diffuser assembly made of transparent acrylic plastic. The assembly consists of an 5.5 cm long converging-diverging nozzle, 9.5 cm long rectangular channel MHD section, and 10 cm long diffuser section. The side walls of the MHD section (same as the nozzle contoured walls) are diverging at 0.5° each to provide boundary layer relief. The channel height and width at the MHD section entrance are 40 mm and 22 mm, respectively. The flow Mach number in the MHD section can be changed between M=3 and M=4 by replacing the nozzle and diffuser inserts shown in Fig. 1.

The MHD test section schematic is shown in Fig. 2. Two rectangular plate copper DC electrodes 4.5 cm long and 2 cm wide, each placed into a boron nitride electrode holder, are flush mounted in the top and bottom walls of the channel. Two pulsed electrode blocks, with a 5 cm x 3.5 cm x 0.3 cm rectangular plate copper electrode sandwiched between mica ceramic blocks and acrylic plastic plates are flush mounted in the side walls, as shown in Fig. 2. The pulsed electrode edges are rounded to achieve a more uniform electric field distribution between the electrodes. The gaps between the pulsed electrodes, the ceramic blocks, and the acrylic plates are filled with silicon rubber to prevent corona formation near the high-voltage electrode surface. The test

section is equipped with a stagnation pressure tap in the nozzle plenum and with two static pressure taps located in the side wall, one 4 cm upstream of the DC electrode and the other is 1 cm downstream of the DC electrode. Static pressure in the test section was monitored using a high accuracy Omega PX811-005GAV pressure transducer, at a sampling rate of 67 Hz. Optical access to the test section is provided by four pairs of rectangular UV grade fused silica windows (Esco Products) placed into the test section walls 1.5 cm upstream and 1.5 cm downstream of the DC electrodes, as shown in Figs. 1,2. This allows optical emission measurements along both horizontal and vertical line-of-sight.

The wind tunnel operates using a 1200 ft^3 dump tank pumped down to 35-40 torr by an Allis-Chalmers 1900 cfm rotary vane vacuum pump. Because of the high back pressure, limited by the vacuum pump cutoff, a step angle diffuser was used downstream of the supersonic test section. The diffuser geometry was determined iteratively, by machining the diffuser inserts to increase the diffuser throat height and to reduce the step angles, until the flow Mach number in the test section, calculated from the static to plenum pressure ratio, became close to the design Mach number. This procedure was used for both M=3 and M=4 diffusers. The resultant ratio of the diffuser height, h_D, to the supersonic test section height, h_T, and the diffuser step angle are h_D/h_T=0.69 and α_d=6° for the M=3 diffuser, and h_D/h_T=0.63 and α_d=5° for the M=4 diffuser. At these conditions, plenum pressure and test section static pressure for the M=3 nozzle / diffuser are P_0=250 torr and P_{test}=9 torr, and those for the M=4 nozzle / diffuser are P_0=600 torr and P_{test}=4.8 torr. This corresponds to the flow Mach number of M=2.80 and M=3.85, respectively. The nozzle throat dimensions are 40 mm x 4.8 mm for the M=3 nozzle and 40 mm x 1.8 mm for the M=4 nozzle, which gives mass flow rates of $\dot{m}$=15 g/sec and $\dot{m}$=14 g/sec, respectively. The entire nozzle / test section / diffuser assembly is placed between the poles of a GMW water cooled electromagnet. In the present experiments, for the 6.5 cm distance between the 15 cm diameter poles, the magnetic field at maximum current through the magnet coils of 140 A is B=1.63 T. A 10 mm diameter circular hole drilled in the center of each magnet pole provides optical access to the test section through the side walls fused silica windows. The magnetic field direction can be switched by changing the magnet power supply polarity. In the present work, two transverse magnetic field directions are referred to "east" and "west", respectively.

A high voltage, short pulse duration, high repetitive rate pulse generator (FID GmbH, FPG 60-100MC4) is used for the generation of the plasma in the test section. The pulse generator

incorporates high voltage step-up circuits triggered by a fast semiconductor switch, Fast Ionization Dynistor (FID) [5]. The pulser generates high voltage, nanosecond duration pulses (peak voltage 8 kV, pulse duration 4 nsec, FWHM) at a pulse repetition of up to 100 kHz. The pulser has four high-voltage output channels, two of them positive polarity and the other two negative polarity. In the present work, the pulser is operated in two different modes, two-channel and four-channel. The first mode is using two output channels (one positive and one negative) connected to the pulsed electrodes in the MHD section by two 3 m long, 75 Ω coaxial transmission cables, so that two opposite polarity pulses (+8 kV and -8 kV) are sent to the load simultaneously, thereby doubling the incident pulse voltage on the electrodes. In the second mode, four output channels are connected to a four 75 Ω cable assembly, in which the central wire of one positive polarity cable is connected to the shielding of the other positive polarity cable before the load, and the same connection is used for the negative polarity cables. This connection doubles both the positive and the negative voltage pulse amplitude (to +16 kV and -16 kV, respectively), so that the incident pulse voltage on the electrodes is quadrupled. Note that the actual voltage between the electrodes may be higher than 16 kV and 32 kV for the two-channel and four-channel modes, respectively, because of the incident pulse reflection. In the absence of the load (i.e. when the cables are disconnected from the pulsed electrodes and then the entire high-voltage pulse is reflected), the positive-to-negative voltage at the end of the transmission cables is 32 kV and 64 kV, respectively.

Transverse DC current (sustainer current) in the supersonic flow ionized by the repetitively pulsed discharge is sustained by applying a DC field (up to 500 V/cm) to two DC electrodes flush mounted in the top and bottom nozzle walls, perpendicular both to the flow velocity and to the magnetic field direction, as shown in Fig. 2. The transverse DC field is applied using a DEL 2 kV / 3A power supply operated in a voltage stabilized mode, with a 0.5 kΩ ballast. Two inductors 1 mH each are placed in the DC circuit in series with both DC electrodes to attenuate high amplitude current pulses propagating into the DC circuit. Current in the DC sustainer circuit is measured using a Tektronix AM503S current probe. The DC current direction (referred to "up" and "down" here) can be changed by switching the power supply polarity.

As discussed in our previous work [3], generation of decelerating and accelerating Lorentz force using two combinations of current and magnetic field vectors for each is essential

30

to isolation of the Lorentz force effect from the Joule heating effect. If the Lorentz force interaction indeed results in significant flow acceleration, the flow static pressure would decrease for both $\mathbf{j}$ and $\mathbf{B}$ vectors configurations producing an accelerating Lorentz force and increase for the other two configurations producing a retarding Lorentz force. On the other hand, if the electric discharge power at these conditions remains the same, Joule heating would result in a static pressure increase (i.e. Mach number reduction), which would be the same for all four of these cases. In case when both these factors, Lorentz force and Joule heating, generate comparable effects on the flow, the static pressure dependence on the Lorentz force direction should still be apparent.

In the present work, high-voltage pulse voltage is measured by two different methods, using a back current shunt probe [6,7] and a capacitive probe [7-9]. The schematics of the two probes are shown in Figs. 3,4. Both probes are installed 1.3 m from the load in one of a 3 m long transmission cables, to avoid an overlap of an incident pulse generated by the pulser and a pulse reflected from the load. In the current shunt, twelve low inductance, low capacitance 3 Ω resistors (Xicon SMD chip resistors) are placed in the 1 cm gap cut in the cable shielding, along the circumference of the dielectric material separating the center wire and the shielding of the cable. The resistance of the shunt is $R_{shunt}=0.25$ Ω. When a high voltage pulse, $U_p(t)$, propagates through the transmission cable, current pulses of the same magnitude, $I(t)=U_p(t)/Z_{trans}$, propagate in the opposite directions through the central wire and the shielding. Here $Z_{trans}=75$ Ω is the transmission cable impedance. The voltage drop on the shunt is measured using a BNC coaxial cable ($Z_{BNC}=50$ Ω) connected in series with a $R_{match}=49.8$ Ω impedance matching resistor (Xicon SMD chip), connected to a Lecroy Wavepro 7100A, 1GHz bandwidth oscilloscope with a $R_{term}=50$ Ω terminator, as shown in Fig. 3. This resistive voltage divider circuit allows avoiding voltage pulse reflections at the terminator and at the shunt. The pulse voltage is calculated as follows,

$$U_p(t) = \frac{Z_{BNC} + R_{match}}{Z_{BNC}} \frac{Z_{trans}}{R_{shunt}} U_{scope}(t) , \qquad (1)$$

where $U_{scope}(t)$ is a voltage signal on the oscilloscope, i.e. the pulse voltage is attenuated by a factor of 600. The current shunt was calibrated using a 250 V amplitude, 10 nsec rise time rectangular voltage pulse generated by a custom-made calibration pulse generator.

Figure 4 shows a schematic and an equivalent circuit of the capacitive probe, which operates as a capacitive voltage divider circuit. The feed-through capacitor is custom made of a 1.5 mm x 1.5 mm square copper plate (contact surface) soldered to the tip of a copper wire (central wire of a 50 Ω BNC coaxial cable), insulated by a multi-layer piece of Kapton tape 1 cm wide wrapped around it, and covered with a copper tape sleeve soldered to the shield line of the BNC cable, as shown in Fig. 4. The capacitor is placed into a channel made in the dielectric material between the central wire and the shielding of the 75 Ω high-voltage pulse transmission cable, as shown in Fig. 4. The distance from the central wire of the transmission cable to the contact surface is approximately 1 mm. Stray capacitances between the contact surface and the central wire, C_p, and between the contact surface and the shielding, C_c, such as $C_c \ll C_p$, are shown in Fig. 4. The BNC cable, in series with a $R_{match}=49.8$ Ω impedance matching resistor, is connected to the oscilloscope through a terminator, $R_{term}=50$ Ω. When a high voltage pulse propagating along the transmission cable arrives at the location of the contact surface, the stray capacitors charge and then discharge through the terminator. The pulse voltage is determined from the voltage on the capacitor C_c, measured by the oscilloscope, as follows [7],

$$U_p(t) = A \frac{Z_{BNC} + R_{out}}{Z_{BNC}} \left(U_{scope}(t) + \frac{1}{\tau} \int_0^t U_{scope}(t')dt' \right), \tag{2}$$

where

$$\tau = (Z_{BNC} + R_{match})(C_c + C_p) \tag{3}$$

$$A = \frac{C_p + C_c}{C_c}$$

are the RC circuit time constant and the voltage divider circuit coefficient, $\tau=0.26$ ns and $A=100$, determined using the same 250 V, 10 nsec rise time calibration pulse.

Flow temperature downstream of the MHD test section was inferred from the nitrogen second positive band emission spectra taken using a 5 m long optical fiber (BFL22-200, Thorlabs) with collimators at each end, and a Princeton Instruments Optical Multichannel Analyzer (OMA) with a 0.5 m monochromator, 1200 g/mm grating, and an ICCD camera. Field of view of the optical fiber was mapped using a point light source (~0.2 mm aperture), which showed the signal collection region to be a cylinder 2-3 mm in diameter and at least 50 mm long, with signal contribution along the line of sight being very nearly constant. Therefore, for a vertical line-of-sight emission measurement, the signal collection region incorporates both the supersonic core flow and the boundary layers downstream of DC electrodes, while for a horizontal line-of-sight measurement, the signal is collected from the supersonic core flow and from the boundary layers downstream of the pulsed electrodes. Rotational temperature of the flow was inferred using a synthetic spectrum [3] with the accurate nitrogen molecular constants, rotational like intensities, and the experimentally measured slit function of the spectrometer.

3. MHD modeling code

In the present work, numerical simulation of the flow in the supersonic nozzle, MHD test section, and the diffuser was done using a 3-D compressible Navier-Stokes / MHD flow code developed by Gaitonde and described in detail in Refs. [10,11]. The governing equations in a non-dimensional form with Lorentz force and energy interaction terms are written as follows,

$$\frac{\partial \rho}{\partial t} + \nabla \cdot (\rho \vec{U}) = 0 \tag{4}$$

$$\frac{\partial \rho \vec{U}}{\partial t} + \nabla \cdot \left[\rho \vec{U}\vec{U} + p\bar{I} \right] - \frac{1}{\mathrm{Re}} \nabla \cdot \bar{\tau} = Q\left(\vec{j} \times \vec{B} \right) \tag{5}$$

$$\frac{\partial \rho e}{\partial t} + \nabla \cdot \left[(\rho e + p)\vec{U} - \frac{1}{\mathrm{Re}}\left(\vec{U} \cdot \bar{\tau} \right) - \frac{1}{(\gamma-1)\mathrm{Pr}\, M^2\, \mathrm{Re}} Q_{ht} \right] = \alpha Q\left(\vec{E} \cdot \vec{j} \right) \tag{6}$$

$$e = \frac{p}{(\gamma-1)\rho} + \frac{\vec{U}^2}{2}, \tag{7}$$

where t is the time, ρ is the density, $\vec{U}$ is the velocity vector, p is the pressure, $\vec{B}$ and $\vec{E}$ are the magnetic and the electric fields, respectively, Q_{ht} is the heat conduction term, $\bar{I}$ and $\bar{\tau}$ are identity and shear stress tensors, respectively, and α is the effective Joule heating factor (the discharge energy fraction going into Joule heating of the flow) [3]. The non-dimensional parameters are the Reynolds number, Re, the Prandtl number, Pr, the Mach number, M, and the interaction parameter $Q=\sigma_{ref}B_{ref}^2L_{ref}/(\rho_{ref}U_{ref})$, where σ_{ref} is the electrical conductivity and L_{ref} is the reference length (nozzle throat height). The rest of the reference parameters are parameters in the nozzle throat. Capabilities of the code include full coupling of Navier-Stokes equations with Maxwell's equations [11] and the use of generalized Ohm's law with tensor electrical conductivity incorporating the ion-slip parameter for the low magnetic Reynolds number approximation. However, in the present work transverse magnetic field and transverse electric field, as well as the flow conductivity in the crossed discharge in the MHD section are assumed to be uniform, and the Hall effect is neglected. Transverse electric field was estimated from the DC voltage and the effective flow conductivity, σ_{eff}, was determined from the current voltage characteristic of the DC discharge (see Section 4), so that transverse current was calculated simply as $j=\sigma_{eff}E$.

The computational domain extends from the nozzle throat, where the flow is assumed to be uniform at M=1, to the end of the diffuser section, where zero axial gradient boundary conditions are imposed. The wall boundary conditions are no-slip, zero pressure gradient, and constant wall temperature (T=300 K) conditions. The number of mesh points in the flow direction (x), magnetic field direction (y), and electric field direction (z) is 151, 61, and 51, respectively. Initial conditions are obtained from a quasi-one-dimensional isentropic expansion flow based on the area ratio. The system of Eqs. (4-7) is solved using a first order Beam-Warming method with fourth order Roe-averaged fluxes, until steady state is reached. Further discussion of time-marching strategy and spatial discretization can be found in Ref. [10] and references therein.

4. Results and Discussion

Figure 5 shows a photograph and a schematic of an oblique shock system in the M=4 diffuser section visualized by the high voltage repetitively pulsed discharge generated in the

MHD section. In the present experiments, the pulser-sustainer discharge appears diffuse and volume filling. However, somewhat brighter emission is observed near the side walls (top and bottom walls in the photograph), i.e. close to the pulsed electrodes, and in the center of the test section. Note that the oblique shocks do not extend through the boundary layer to the test section walls. A linear extrapolation of the shock fronts suggests that the oblique shocks originate somewhat upstream of the 5.5° diffuser step angles, possibly due to flow separation at the compression corners. The oblique shock wave angle determined from the photograph is approximately $\beta=19°$, which corresponds to the flow Mach number at the end of the test section of M=3.85. This is consistent with the static pressure measurements downstream of the MHD section, P=4.8 torr for the stagnation pressure of $P_0=600$ torr, which also corresponds to M=3.85.

Figure 6 shows incident and reflected high voltage pulses for a single pulse generated during the two-channel pulser operation at atmospheric pressure in the test section, measured by the capacitive probe and by the current shunt. At these conditions, there is no breakdown in the test section, so that the entire pulse is reflected. Incident pulse peak voltages (at t=30 nsec) measured by the capacitive probe and by the current shunt are 8.1 kV and 8.3 kV, respectively, while reflected pulse peak voltages (at 50 nsec) are 7.0 kV and 8.0 kV, respectively. Although the peak incident pulse voltage measured by the capacitive probe is somewhat lower than that measured by the current shunt, both measurements resulted in almost the same FWHM of 4.2 ns, rise time of 1.6 ns, and fall time of 1.8 ns. Estimated pulse energy coupled to the load at these conditions, calculated as the difference of the incident and the reflected pulse energies [7,12],

$$W = \int_0^\tau \frac{U_{inc}(t)^2}{Z_{trans}} dt - \int_0^\tau \frac{U_{ref}(t)^2}{Z_{trans}} dt \qquad (8)$$

is 0.5 mJ / channel from the capacitive probe signal and 0.3 mJ / channel from the current shunt probe signal. In Eq. (8), $Z_{trans}=75\ \Omega$ is the transmission cable impedance. Both numbers are close to each other and are much lower than the incident pulse energy, 3.1 mJ. Note that this result provides an estimate of the uncertainty in the coupled pulse energy measurement. The capacitive probe bandwidth, estimated using the same method as in Ref. [7], is ~20 GHz, above which the inductance of the feed-through capacitor may affect the signal. On the other hand, transition frequency of chip resistors used in the current shunt is significantly lower, of the order of 1 GHz,

above which their reactivity starts affecting the signal. Also, the reflected pulse measured by the current shunt at the conditions when plasma was generated between the electrodes was very noisy. Because of this, we used the capacitive probe for further incident and reflected pulse energy measurements.

Figure 7 shows incident and reflected pulses measured by the capacitive probe in a two-channel pulsed discharge at pulse repetition rate of $v=100$ kHz, for the 1st pulse and for the 4000th pulse (i.e. 40 ms later). These measurements are taken in a M=4 nitrogen flow at $P_0=600$ torr, $P_{test}=4.8$ torr, and B=1.63 T. It can be seen that the incident pulse peak voltage is 8.1 kV for the 1st pulse and 7.0 kV for the 4000th pulse, while the reflected pulse voltage also decreases. The pulse voltage decrease may be due to residual charge accumulation in the transmission cable and on the pulsed electrodes. Pulse energy coupled to the plasma, calculated from the waveforms of Fig. 7, is 1.1 mJ / channel for the 1st pulse and 0.6 mJ / channel for the 4000th pulse. This corresponds to 60 W / channel time averaged discharge power at $v=100$ kHz at the steady state conditions (i.e. 240 W for the four channel operation). However, note that since the coupled pulse energies are rather low and comparable with the coupled pulse energy measured in the absence of the plasma (0.5 mJ / channel), this result has a large uncertainty and could be significantly lower. Basically, these measurements suggest even when a plasma is sustained between the pulsed electrodes, most of the incident pulse energy (at least 80%) is reflected. For comparison, in our previous coupled pulse energy measurements in a M=3 nitrogen flow at B=1.5 T [3] using the CPT pulse generator (peak voltage 13-15 kV, pulse duration 30 ns, pulse repetition rate $v=40$ kHz), coupled pulse energy was about 1 mJ and the time averaged discharge power was approximately 40 W.

Figure 8 shows oscillograms of DC sustainer current in a M=4 nitrogen flow at $P_0=600$ torr, $P_{test}=4.8$ torr, and B=1.63 T, ionized by a $v=100$ kHz four-channel pulsed discharge. In Fig. 8, DC power supply voltage is $U_{PS}=\pm1.4$ kV and a ballast resistance is R=0.5 kΩ. It can be seen that the sustainer current peaks at I=1.2 A approximately 3 µs after each ionizing pulse, and decays to I=0.75 A before the next pulse. For both DC voltage polarities, the time-averaged sustainer currents are very close, <I>=0.94 A and 0.93 A, respectively. This corresponds to the time-averaged voltage between the electrodes, <U> = U_{PS}-<I>R = 0.93 kV and the DC discharge power of 0.87 kW. For comparison, in our previous measurements in M=3 nitrogen and air flows [3], ionized by a CPT pulser at $v=40$ kHz, the DC discharge current, voltage and power were

36

<I>=0.9 A, <U>=1.6 kV, and 1.4 kW, respectively. It can be seen that flow ionization by the FID pulser operated in the four-channel mode produces comparable sustainer currents at significantly lower DC voltages, i.e. the FID pulser generates higher flow conductivity.

This effect is further illustrated by comparing current-voltage characteristics of the sustainer discharge for the two-channel and four-channel operation modes of the FID pulser (ν=100 kHz) in a M=4 nitrogen flows, and for the CPT pulser in a M=3 nitrogen flow ionized by the CPT pulser (ν=40 kHz) [3], both measured in magnetic field of B=1.5 T (see Fig. 9). The effective electrical conductivities for these two cases were determined from linear fits to the current-voltage characteristics, as shown in Fig. 9, σ_{eff}=0.04 S/m for the M=3 flow / CPT pulser, and σ_{eff}=0.1 S/m for the M=4 flow / four-channel FID pulser. We conclude that the flow conductivity generated by the FID pulser is indeed significantly higher, by about a factor of 2.5. Note that the scalar flow conductivity, i.e. the conductivity at B=0, is somewhat higher, since in the presence of magnetic field the conductivity is reduced due to the Hall effect.

Figure 10 shows plasma emission spectra, 1→4 band of nitrogen second positive system ($C^3\Pi_u$→$B^3\Pi_g$), averaged along the horizontal line-of-sight by the optical fiber, taken in the repetitively pulsed discharge with and without DC voltage applied. The flow conditions in Fig. 10 are nitrogen at P_0=600 torr, P_{test}=4.8 torr, B=1.5 T, with a four-channel pulsed discharge operating at ν=100 kHz. The DC power supply voltage was U_{PS}=1.3 kV. It can be seen that the two spectra are very close to each other, suggesting that flow temperature increase due to the DC discharge is small. As discussed in our previous work [3], at the reduced electric field in the sustainer discharge, E/N=(3-4)·10^{-16} V·cm^2 (based on the isentropic core flow temperature), most of the discharge energy, up to 90%, goes to vibrational excitation of nitrogen and remains "locked" there due to its slow vibrational relaxation. Figure 11 compares the experimental spectrum without DC voltage applied with two synthetic spectra, one for the M=3.85 isentropic core flow temperature of T=77 K, and the other is the horizontal line-of-sight averaged spectrum for the temperature distribution predicted by the 3-D Navier-Stokes code with the Lorentz force and Joule heat turned off (see Fig. 12). One can see that the two synthetic spectra are very close, demonstrating that the contribution of warm boundary layers into the line-of-sight spectrum is insignificant. On the other hand, both synthetic spectra somewhat underpredict the flow temperature, since the tail of the experimental spectrum is higher than that of the synthetic spectra.

Figure 13 shows normalized test section static pressure traces measured in a M=4 nitrogen flow at the plenum pressure of P_0=600 torr, with and without Lorentz force applied at the magnetic field of B=1.63 T. As in our previous work [3], static pressure was measured for both accelerating and decelerating Lorentz force directions, each generated by two different combinations of transverse B field and transverse current directions. This was done to isolate the polarity-dependent Lorentz force effect from the polarity-independent Joule heat effect. Turning the pulser on in the presence of magnetic filed, without applying transverse DC electric field, i.e. generating ionization in the test section without applying Lorentz force resulted in a static pressure increase by 2-3% from the baseline pressure of 4.8 torr, due to Joule heating generated by the pulser (see Fig. 13). The other four pressure traces plotted in Fig. 13 correspond to four different combinations of transverse current vector and magnetic field vector directions, east/up, west/down (both producing accelerating force), west/up, and east/down (both producing retarding force).

As in our previous measurements, the static pressure increased for all four combinations. However, the pressure rise for both accelerating force configurations was higher than for both retarding force configurations (see Fig. 13). Normalized static pressure rise for the retarding and for the accelerating Lorentz force was $\Delta P_R/P$=1.19±0.03 and $\Delta P_A/P$=1.11±0.03, for the same time-averaged DC currents of <I>=0.93-0.94A, as shown in Fig. 9. The normalized baseline pressure (with no Lorentz force applied) was 1.00±0.03. This effect is consistent with our previous results [3] obtained in M=3 nitrogen and air flows ionized by the CPT pulse generator. Basically, static pressure increases due to Joule heating, which is nearly identical in all four cases (see Fig. 8). However, flow acceleration by the Lorentz force reduces the pressure rise, while flow deceleration increases it. Note, however, that in spite of the higher flow conductivity achieved in the present work (a factor of 2.5 higher than in M=3 flows, see Fig. 9), the Lorentz force effect on the static pressure is somewhat lower than in our previous work [3]. From the results of Fig. 13, the effective Joule heating factor (i.e. the discharge energy fraction going into Joule heating of the flow) [3],

$$\alpha \cong \frac{\Delta P_A + \Delta P_R}{2} \frac{M^2 - 1}{(\gamma - 1)M} \frac{a}{j_y E_y L} \tag{9}$$

is $\alpha \approx 0.2$. In Eq. (9), $j_y = 0.093$ A/cm^2 is transverse current density, $E_y = 230$ V/cm is transverse electric field, L=4.5 cm is the length of the MHD section, M=3.85, $\gamma = 1.4$, and a=297 m/s is the speed of sound at T=77 K. At the present experimental conditions, the effective loading parameter, i.e. the ratio of Joule heating to the Loretnz force work is $K = \alpha E_y / MaB \approx 4.2$, is nearly the same as in our previous work in M=3 flows, $K \approx 4$.

To verify whether the static pressure change shown in Fig. 13 is indeed caused by the flow acceleration and deceleration by the Lorentz force, we used the 3-D Navier-Stokes / MHD flow code briefly described in Section 3. In the calculations, experimental values of flow conductivity, $\sigma_{eff} = 0.1$ S/m, transverse electric field, E=200 V/cm, magnetic field, B=1.5 T, and effective Joule heating factor, $\alpha = 0.2$, were used as entries in the code. Figure 14 shows a contour plot of the Mach number distribution in the M=4 nozzle / test section / diffuser for the baseline conditions, $P_0 = 600$ torr and without plasmas and magnetic field. It can be seen that the Mach number in the test section peaks at M=3.85, which is consistent with the number inferred from the static pressure measurements. Two flow separation regions formed upstream of the diffuser angle steps, weak compression waves in the test section, and oblique shocks in the diffuser are also visible in Fig. 13.

Figure 15 shows axial flow velocity distribution across the flow cross section at the end of the discharge section, for both accelerating and decelerating Lorentz force directions. In this figure, boundary layer bulges formed on the plane walls due to the secondary cross flow are clearly visible. This effect was detected experimentally in our previous work [3], as well as in previous 3-D flow modeling calculations [4]. Although at the present conditions the difference between the accelerated and decelerated flow fields is small, one can see that decelerating force results in the increase of flow separation bubbles inside the boundary layer bulges, as well as in thicker boundary layers on the contoured walls (see Fig. 15).

Figure 16 shows static pressure along one of the plane walls, predicted by the code for baseline, accelerated, and decelerated flows, as well as experimental results such as shown in Fig. 13. One can see that the code somewhat overpredicts the static pressure in the test section (by 10-20%). However, static pressure rise downstream of the MHD section, predicted by the code, is consistent with the experimental measurements. In particular, the predicted pressure rise in the flow decelerated by the Lorentz force is greater than the pressure rise in the accelerated flow, by approximately the same amount. Normalized static pressure rise for the retarding and

for the accelerating Lorentz force, predicted by the code, is $\Delta P_R/P=1.18$ and $\Delta P_A/P=1.08$. This result provides further evidence that the static pressure change detected in the present experiments, as well as in our previous work [3], is indeed due to MHD effect.

Figure 17 plots axial velocity for the same three cases as shown in Fig. 16. It can be seen that for the accelerating Lorentz force direction, combination of Joule heating (which decelerates a supersonic flow) and accelerating body force cancel each other and result in a near zero net velocity change. On the other hand, these two effects are combined for the retarding Lorentz force direction, resulting in a velocity reduction by approximately $\Delta u=15$ m/sec at the end of the MHD section (about 2% velocity reduction). Although the predicted flow deceleration is small, we believe that it can be detected by using Molecular Tagging Velocimetry (MTV) optical diagnostics. In this technique, the flow is seeded with a small amount of NO, and the excited electronic state of nitric oxide, $NO(A^2\Sigma)$, is populated by resonance absorption of a pump laser beam at 226 nm. Fluorescence of $NO(A^2\Sigma)$ back to the ground electronic state is monitored after a 0.2-0.6 μsec delay after the laser pulse. Previous MTV experiments [13] suggests that the uncertainty in the M=2 flow velocity measurements using this technique can be only about ~1-2 m/sec. Therefore the MHD flow deceleration effect may well be detected using this diagnostics. These experiments are currently underway.

5. Summary

The paper presents results of cold MHD flow deceleration experiments using repetitively pulsed, short pulse duration, high voltage discharge to produce ionization in a M=4 nitrogen flow in the presence of transverse DC electric field and transverse magnetic field. Effective flow conductivity is significantly higher than was previously achieved, $\sigma_{eff}=0.1$ S/m. MHD effect on the flow is detected from the flow static pressure measurements. Retarding Lorentz force applied to the flow produces a static pressure increase of 19%, while accelerating force of the same magnitude applied to the same flow results in static pressure increase of 11%. The effect is produced for two possible combinations of the magnetic field and transverse current directions producing the same Lorentz force direction (both for accelerating and retarding force). The results of static pressure measurements are compared with predictions of a 3-D Navier-Stokes / MHD flow code. The fraction of the discharge input power going into Joule heat has been inferred from the present experiments, and used as one of the input parameters in the MHD flow

40

model. The static pressure rise predicted by the code, 18% for the retarding force and 8% for the accelerating force, agrees well with the experimental measurements. Analysis of the calculations results shows that at the present conditions, the effects of Joule heating and the accelerating Lorentz force cancel each other, producing nearly zero net flow velocity change. On the other hand, the two effects are combined for the retarding Lorentz force, which results in approximately 2% flow velocity reduction, by $\Delta u=15$ m/sec. This result provides further evidence of cold supersonic flow deceleration by Lorentz force. The present results suggest that this effect can be detected by Molecular Tagging Velocimetry (MTV) optical diagnostics, which has an uncertainty of about 1-2 m/sec.

References

1. M. Nishihara, N. Jiang, J.W. Rich, W.R. Lempert, I.V. Adamovich, and S. Gogineni, "Low-temperature supersonic boundary layer control using repetitively pulsed magnetihydrodynamic forcing," Physics of Fluids, Vol. 17, 2005, pp. 106102-106102-12

2. R.C. Murray, S.H. Zaidi, M.R. Carraro, L.M. Vasilyak, S.O. Macheret, M.N. Shneider, and R.B. Miles, "Magnetohydrodynamic Power Generation Using Externally Ionized, Cold, Supersonic Air as Working Fluid", AIAA Journal, vol. 44, No. 1, 2006, pp. 119-127

3. M. Nishihara, J.W. Rich, W.R. Lempert, I.V. Adamovich, and S. Gogineni, "Low-temperature M=3 flow decelerations by Lorentz force," Physics of Fluids, Vol. 18, 2006, pp. 086101-086101-11.

4. P. Rawat, X. Zhong, V. Singh, and S. Gogineni, "Numerical Simulation of Secondary Flow in a Weakly Ionized Supersonic Flow with Applied Electromagnetic Field", AIAA Paper 2005-5050, 36th AIAA Plasmadynamics and Lasers Conference, Toronto, Ontario, June 6-9, 2005.

5. I.V. Grekhov, S.CV. Korotkov, A.L. Stepaniants, D.V. Khristyuk, V.B. Voronkov, and Y.V. Aristov, "High-power semiconductor-based nano and subnanosecond pulse generator with a low delay time," IEEE Transactions on Plasma Science, Vol. 33, 2005, pp. 1240-1244.

6. L.M. Vasilyak, S.V. Kostyuchenko, A.V. Krasnochub, N.N. Kudryavtsev, and G.A. Kurkin, "An experimental investigation of the electrodynamic and spectral characteristics

of a nanosecond pulse-periodic discharge in chlorine," High Temperature, Vol. 33, 1995, pp. 822-828.

7. N. Anikin, *Experimental Investigation of Electrodynamic Characteristics of the Fast Ionization Wave in Molecular Gases*, Ph.D. dissertation, Moscow Institute of Physics and Technology, 2000 (in *Russian*).

8. M.M. Brady and K.G. Dedrick, "High-voltage pulse measurement with a precision capacitive voltage divider," The Review of Scientific Instruments, Vol. 33, 1962, pp. 1421-1428.

9. W.R. Fowkes and R.M. Rowe, "Refinements in precision kilovolt pulse measurements," IEEE Transactions on Instrumentation and Measurement, Vol. 15, 1966, pp. 284-292.

10. D.V. Gaitonde, "A high-order implicit procedure for the 3-D electric field in complex magnetogasdyanamic simulations," Computers & Fluids, Vol. 33, 2004, pp. 345-374.

11. D.V. Gaitonde, "High-order solution procedure for three-dimensional nonideal magnetogasdynamics," AIAA Journal, Vol. 39, 2001, pp. 2111-2120.

12. É.I. Asinovskii, L.M. Vasilyak, A.V. Kirillin, and V.V. Markovets, "Nanosecond discharge in a weakly ionized plasma," High Temperature, Vol. 13, 1975, pp. 32-35.

13. W.R. Lempert, M. Boehm, N. Jiang, S. Gimelshein, and D. Levin, "Comparison of molecular tagging velocimetry data and direct simulation Monte Carlo simulations in supersonic micro jet flow," Experiments in Fluids, Vol. 34, 2003, pp. 403-411.
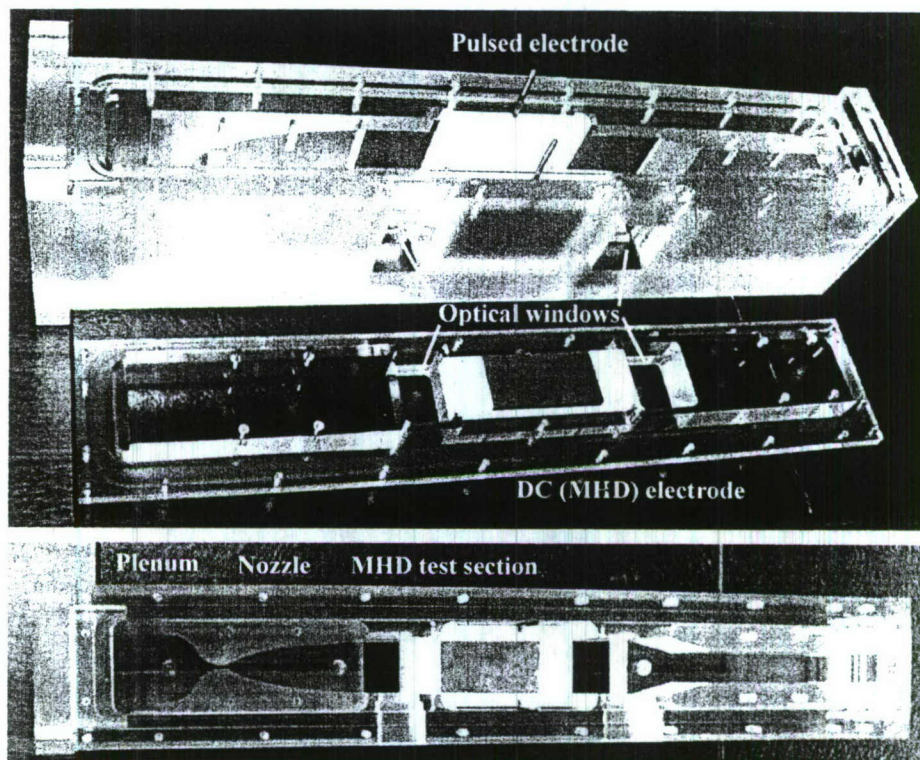
Figure 1. New M=3 / M=4 supersonic nozzle / MHD test section / diffuser assembly, shown with M=4 nozzle inserts in place. Flow is from left to right.
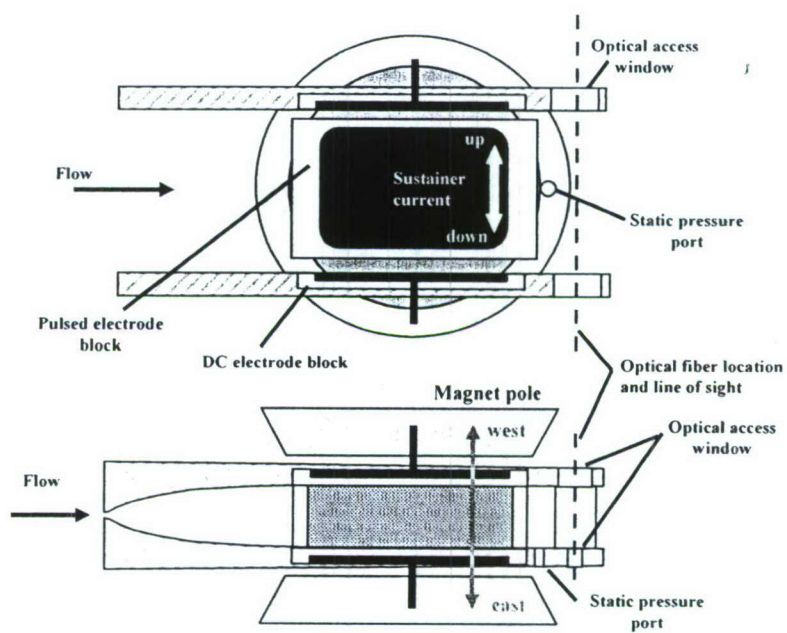
Figure 2. Schematic of a supersonic nozzle and MHD test section.
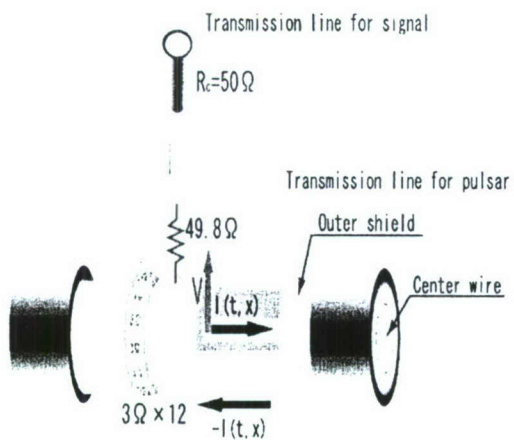
Figure 3. Schematic of a back current shunt.
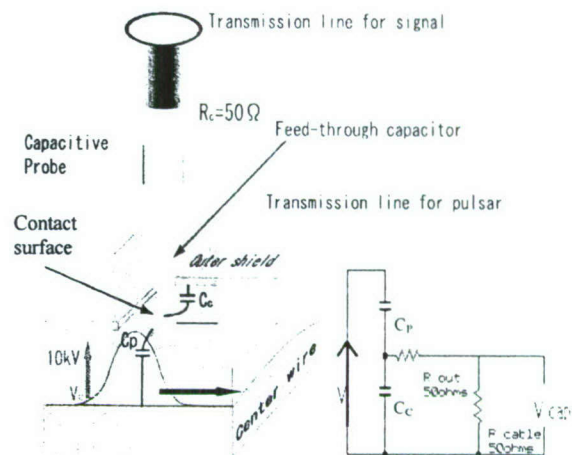
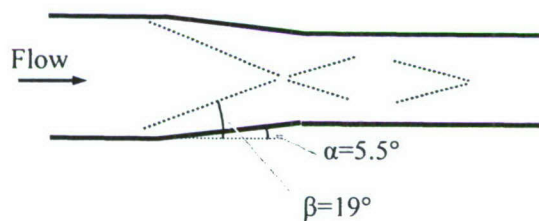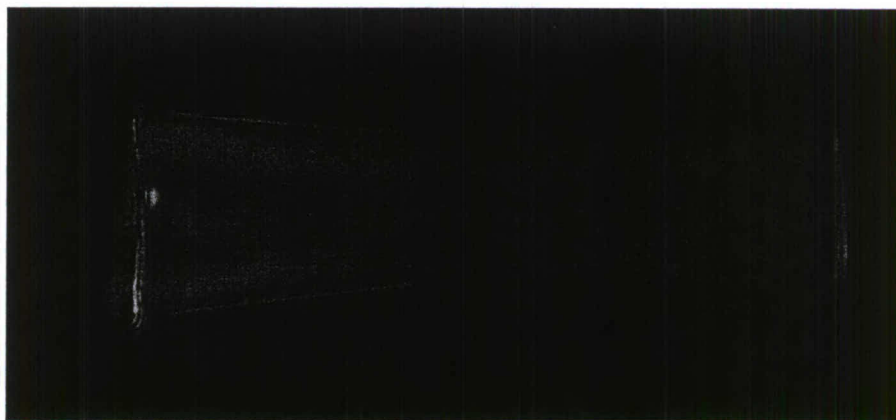**Figure 4.** Schematic and an equivalent circuit of a capacitive probe.

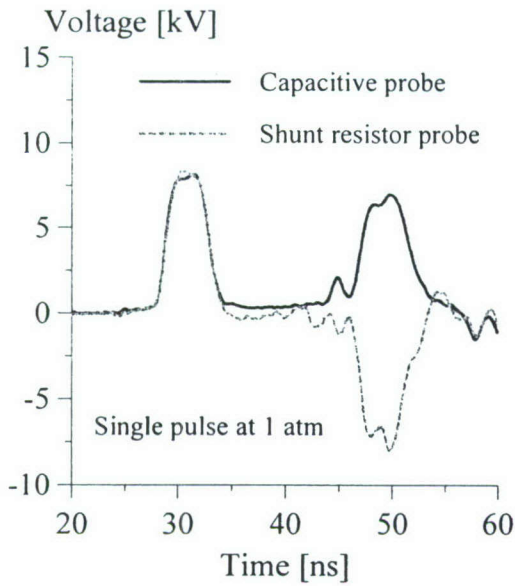**Figure 5.** Photograph and schematic of an oblique shock pattern in the M=4 diffuser. Nitrogen, P_0=600 torr, P_{test}=4.8 torr (M=3.85).

Figure 6. Incident and reflected voltage pulses measured by the capacitive probe and by the back current shunt at the atmospheric pressure in the test section.
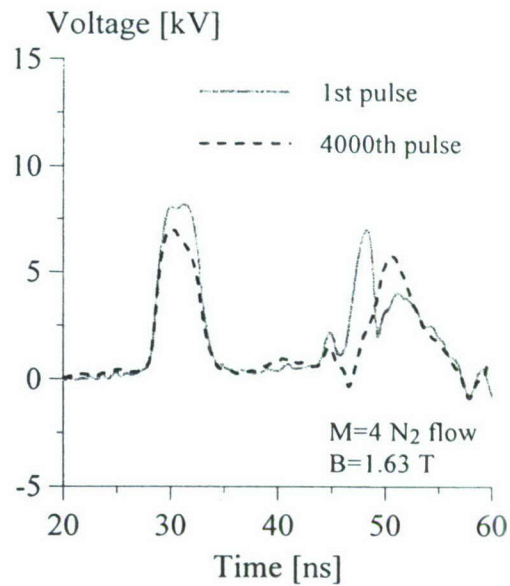
Figure 7. Incident and reflected voltage pulses measured by the capacitive probe for the 1st pulse and for the 4000th pulse. M=4 nitrogen flow, P_{test}=4.8 torr, B=1.63 T, v=100 kHz.
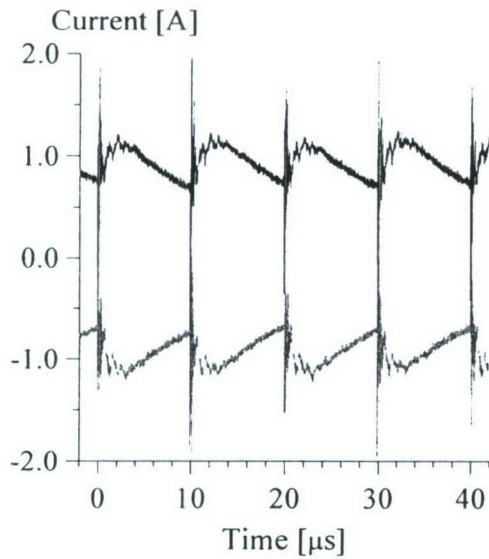
Figure 8. Sustainer current traces for two different transverse DC electric field polarities. M=4 nitrogen flow, P_0=600 torr, P_{test}=4.8 torr, B=1.5 T, v=100 kHz, U_{PS}=1.4 kV, R=0.5 kΩ. Time-averaged currents are 0.94 A (top curve) and 0.93 A (bottom curve).
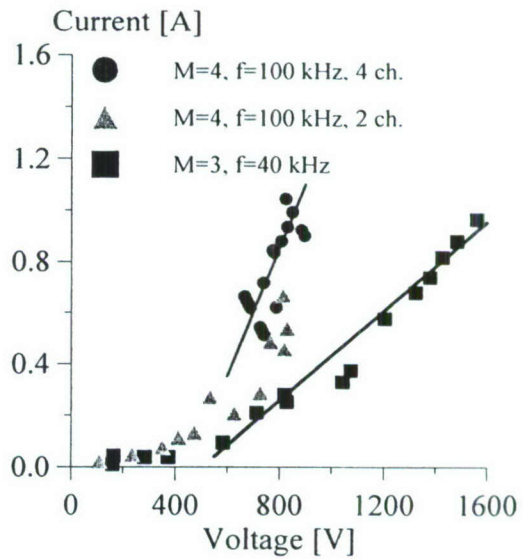
Figure 9. Current voltage characteristics in nitrogen flows at B=1.5 T, for different Mach numbers and different pulser operation modes. For M=3, P_0=250 torr, P_{test}=7.5 torr, v=40 kHz. For M=4, P_0=600 torr, P_{test}=4.8 torr, v=100 kHz.

45

Intensity [arb.]
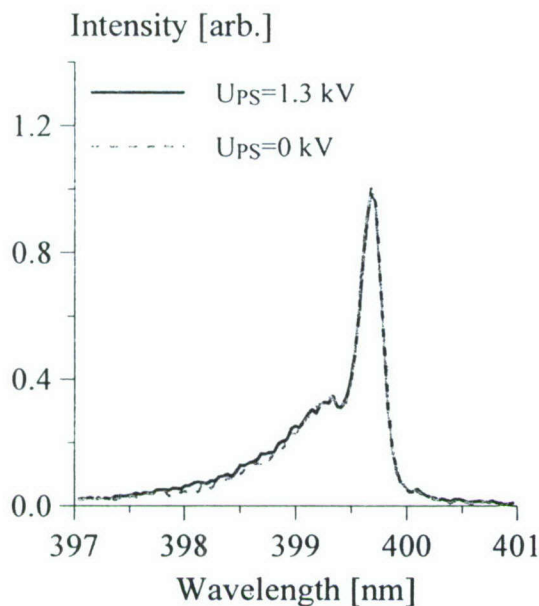
Figure 10. $N_2(C^3\Pi_u \rightarrow B^3\Pi_g)$ emission spectra (1→4 band) measured along a horizontal line-of-sight in a M=4 nitrogen flow at P_0=600 torr, B=1.5 T, and v=100 kHz, with and without 0.9 kW DC sustainer discharge.
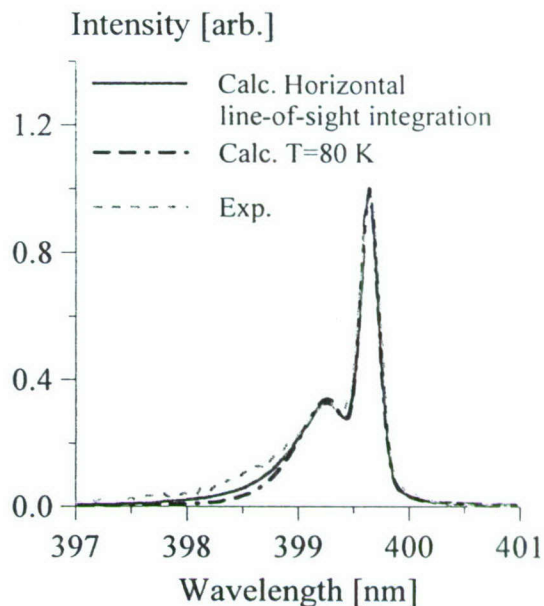
Intensity [arb.]

Figure 11. Comparison of experimental spectrum of Fig. 10 (without DC discharge) and synthetic spectra for T=80 K and for the temperature distribution predicted by the code for the horizontal line-of-sight (see Fig. 12)
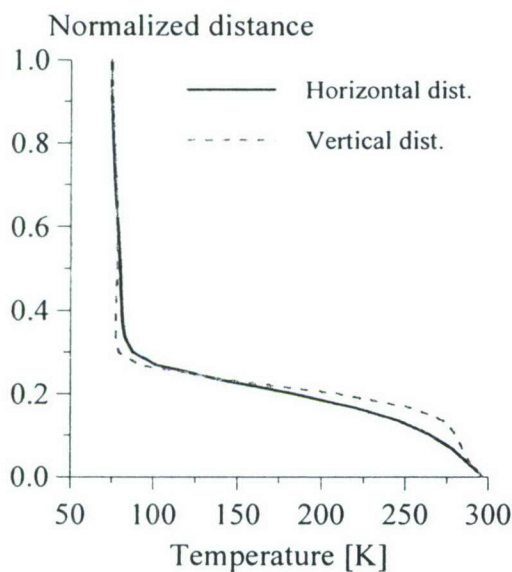
Normalized distance

Figure 12. Static temperature distributions along the horizontal and vertical centerlines in a cold M=4 flow (without Joule heating or Lorentz force).
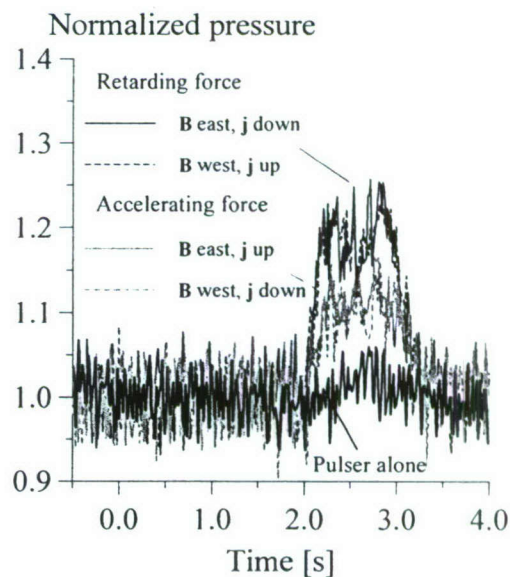
Normalized pressure

Figure 13. Normalized static pressure traces in a M=4 nitrogen flow at P_0=600 torr, P_{test}=4.8 torr, B=1.63 T, v=100 kHz. U_{PS}=1.4 kV, and R=0.5 kΩ. Lorentz force is applied for 1 sec duration.
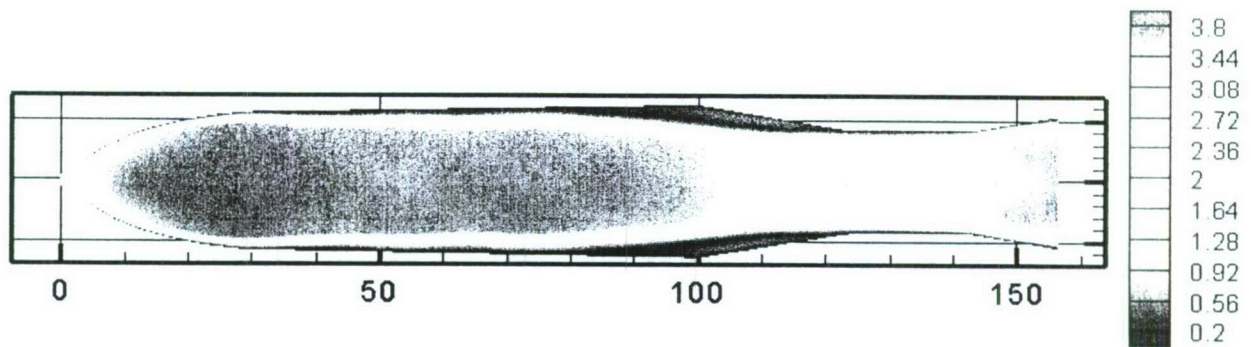
46

Figure 14. Mach number distribution in a baseline M=4 nitrogen flow.
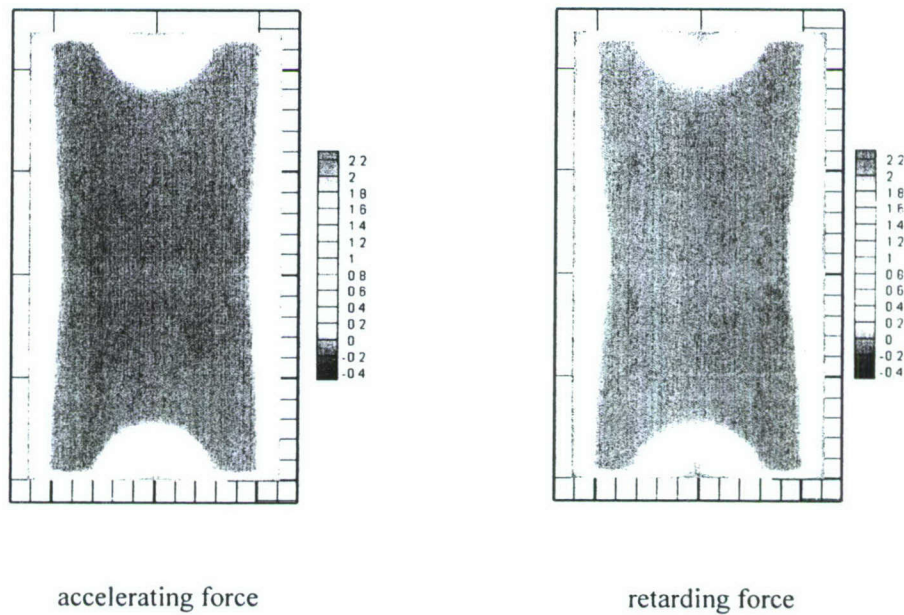

accelerating force   retarding force

Figure 15. Normalized axial velocity distributions at the end of the MHD section for the accelerated and retarding Lorentz force directions.

47

Wall pressure, torr

MHD forcing region

10

8

6

4

2

0

0   2   4   6   8   10 12 14 16 18

baseline
accelerating
decelerating
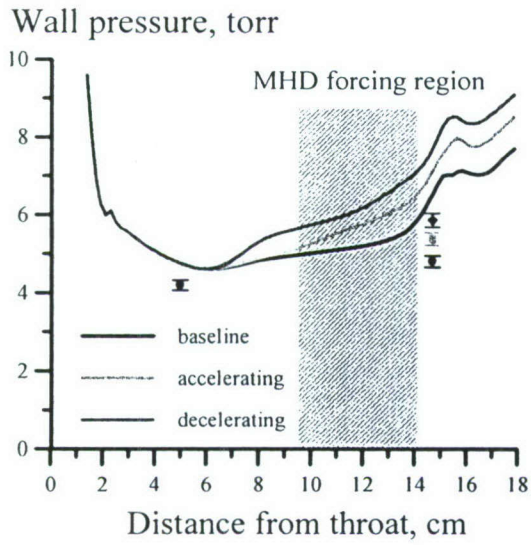
Distance from throat, cm

Figure 16. Static pressure distributions along the side (contoured) wall for the baseline, accelerated, and retarded M=4 nitrogen flows. Location of the pulser-sustainer discharge is shown.
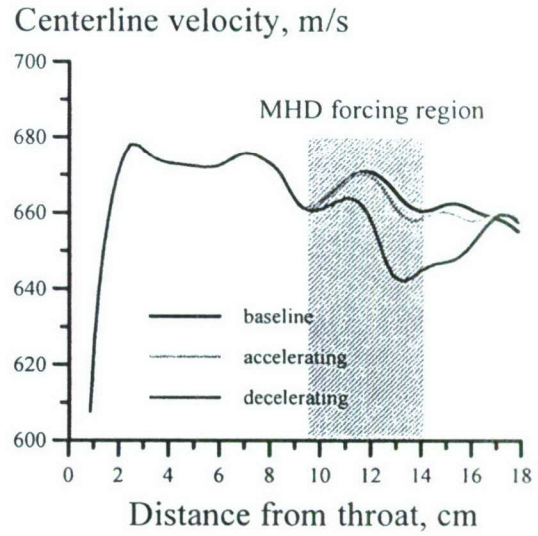
Centerline velocity, m/s

MHD forcing region

700

680

660

640

620

600

0   2   4   6   8   10 12 14 16 18

baseline
accelerating
decelerating

Distance from throat, cm

Figure 17. Centerline axial velocity distributions for the baseline, accelerated, and retarded M=4 nitrogen flows. Location of the pulser-sustainer discharge is shown.

48

CHAPTER III.

NUMERICAL SIMULATION OF A CROSSED PULSER-SUSTAINER DISCHARGE IN TRANSVERSE MAGNETIC FIELD

1. Introduction

In recent years, there has been a significant increase of interest in applications of low-temperature magnetohydrodynamics (MHD) for supersonic flow control, on-board power generation, supersonic air-breathing propulsion, and development of novel hypersonic ground testing facilities [1-14]. One of key factors affecting development and scaling of these applications is the ability to efficiently generate, sustain, and control volume-filling, high electrical conductivity, low-temperature plasmas in high-speed unseeded air flows. As is well known, at these conditions nonequilibrium plasmas are prone to ionization instability development [15]. This results in plasma constriction and formation of high-current, high-temperature arc filaments, resulting in localized heating of the flow, erosion of adjoining surfaces, and reduction of MHD interaction.

One of the most effective ways of nonequilibrium plasma stabilization, first suggested and experimentally demonstrated by Hill [16], is using two overlapping (crossed) electric discharges, one producing a series of high voltage, nanosecond pulse duration, high repetition rate ionizing pulses, and the other providing a below-breakdown DC sustainer voltage. In this method, uniform ionization is produced by repetitive nanosecond pulses, which are far too short for ionization instabilities and arc filaments to develop. Basically, the pulse duration, ~10-100 nsec, is much shorter than the characteristic time for the ionization instability development, ~10^{-3}-10^{-4} sec [15]. Since the DC sustainer voltage is too low to produce ionization, the decaying plasma remains stable between the pulses, while the sustainer voltage draws the electric current and couples power to the plasma. This arrangement is known as a non-self-sustained electric discharge. Uncoupling of ionization and energy addition processes prevents positive feedback between the Joule heating of the plasma and the rate of ionization by electron impact, existing in self-sustained discharge plasmas [15]. This approach has been previously used to develop a large discharge volume, high power, fast flow CO_2 laser [17,15]. From a practical standpoint, external ionization by high-voltage pulses offers key advantage over another well known external

ionization method using a high energy electron beam [18-20], since nanosecond high voltage pulse generators are much simpler in operation and maintenance compared to electron guns.

A renewed interest in aerospace applications of nonequilibrium plasmas in 1990's resulted in significant progress in studies of repetitively pulsed nanosecond discharges. Kinetic modeling calculations [21,22] suggested that this type of discharge can be used for energy efficient ionization in nonequilibrium MHD flows. Uniform nanosecond pulse duration plasmas have been used for generating low power budget, atmospheric pressure air plasmas [23], for low-temperature MHD flow control and power generation [11-13], for plasma assisted combustion [24-26], and for singlet delta oxygen generation in electrically excited oxygen-iodine laser [27-29]. Potential for volume scaling of nanosecond pulse generated high-pressure plasmas has been demonstrated in experiments using fast ionization wave [24,25], where plasma was generated at P~1 atm, across distances of up to tens of cm. Specific advances in low-temperature MHD plasmas sustained by nanosecond pulse ionization include MHD control of density fluctuations in supersonic boundary layer [11], demonstration of supersonic air flow deceleration [12], and demonstration of MHD plasma generation in unseeded air flows [13]. Note that in these experiments, the MHD interaction parameter, defined as the ratio of work by the Lorentz force, $|j_y B_z|L$, to the flow kinetic energy, ρu_∞^2,

$$\eta = \frac{|j_y B_z|L}{\rho u_\infty^2} \tag{1}$$

was fairly low, $\eta \sim 0.01$. The highest steady-state MHD air flow conductivity achieved so far, sustained by high repetition rate ionizing pulses, is of the order of $\sigma \sim 0.1$ Si/m [11].

Further development of low-temperature MHD technology requires better understanding of behavior of repetitively pulsed, non-self-sustained discharge plasmas in magnetic field. The main objectives of the present paper are (i) to obtain insight into kinetics of non-nonequilibrium plasma of a crossed pulser-sustainer discharge in the presence of transverse magnetic field and (ii) to evaluate its potential for the use in MHD flow control and power generation.

2. Two-dimensional pulser-sustainer discharge model

Figure 1 shows a schematic of the integration domain used in the present calculations, incorporating transverse DC discharge sustained by repetitive high voltage ionizing pulses in transverse magnetic field. The size of the integration domain is 9 cm in the horizontal (x) direction by 4 cm in the vertical (y) direction. The direction of the DC electric field is top to bottom, in the negative y-direction. The magnetic field is directed out of the page, in the positive z-direction. This generates Lorentz force on the charged species in the plasma, $jxB=\sigma(ExB)$, directed to the left, in the negative x-direction. If a neutral species flow were taken into account, with the flow direction left to right, Lorentz force would decelerate the flow due to collisional coupling between the charged species (electrons and ions) and the neutral species. In the present calculations, however, the neutral species flow is not considered. This somewhat simplified problem formulation implies weak collisional coupling between the plasma and the neutral flow, i.e. a low MHD interaction parameter (see Eq. (1)). Basically, the effect of the plasma on the flow at the present conditions is considered to be weak.

In the calculations, the pulsed electrodes are modeled by a rectangular shape uniform ionization region, 4.5 cm wide (in the x-direction) and 3 cm tall (in the y-direction). The test section depth (in the z-direction) is 2 cm, and the pulsed electrodes are assumed to be placed 2.4 cm apart. These dimensions are the same as in our previous MHD experiments [11,12]. The pulsed electric field is parallel to magnetic field. Although finite length (5 cm long) DC electrodes have been used in experiments [11,12], in the present calculations the DC electrodes (cathode on the bottom and anode on the top, see Fig. 1) are assumed to be infinitely long. This approach helps avoiding numerical difficulties in the high electric field regions, near the edges of the finite electrodes.

A two-dimensional, time-dependent kinetic model of a nonequilibrium DC electric discharge sustained by repetitively pulsed external ionization in presence of transverse magnetic field incorporates equations for the ion and for the electron densities in the drift-diffusion approximation, as well as the Poisson equation for the electric potential,

$$\frac{\partial n_+}{\partial t} + \frac{\partial \Gamma_{+,x}}{\partial x} + \frac{\partial \Gamma_{+,y}}{\partial y} = \alpha(E_p(t)/N)n_e\,\mu_e E_p + \alpha(E/N)|\Gamma_e| - \beta_{ei}n_+n_e \qquad (2)$$

$$\frac{\partial n_e}{\partial t} + \frac{\partial \Gamma_{e,x}}{\partial x} + \frac{\partial \Gamma_{e,y}}{\partial y} = \alpha(E_p(t)/N) n_e \mu_e E_p + \alpha(E/N)|\Gamma_e| - \beta_{ei} n_+ n_e \qquad (3)$$

$$\frac{\partial^2 \varphi}{\partial x^2} + \frac{\partial^2 \varphi}{\partial y^2} = -\frac{e}{\varepsilon_0}(n_+ - n_e) \qquad (4)$$

In Eqs. (2-4), n_+ and n_e are the ion and the electron number densities, respectively, φ and $E = |\nabla \phi|$ are the potential and the electric field in the DC sustainer discharge, α is the Townsend ionization coefficient by electron impact [30], $E_p(t)$ is the electric field in a high-voltage ionizing pulse, N is the total number density, and β_{ei} is the rate of electron-ion recombination.

In Eqs (2, 3), $\Gamma_{e,x}, \Gamma_{e,y}, \Gamma_{+,x}, \Gamma_{+,y}$ are the x- and the y- components of electron and ion drift-diffusion fluxes [31],

$$\Gamma_{+,x} = \frac{1}{1+\beta_+^2}\left(-D_+ \frac{\partial n_+}{\partial x} + \mu_+ n_+ E_x\right) + \frac{\beta_+}{1+\beta_+^2}\left(-D_+ \frac{\partial n_+}{\partial y} + \mu_+ n_+ E_y\right) \qquad (5)$$

$$\Gamma_{+,y} = \frac{1}{1+\beta_+^2}\left(-D_+ \frac{\partial n_+}{\partial y} + \mu_+ n_+ E_y\right) - \frac{\beta_+}{1+\beta_+^2}\left(-D_+ \frac{\partial n_+}{\partial x} + \mu_+ n_+ E_x\right) \qquad (6)$$

$$\Gamma_{e,x} = \frac{1}{1+\beta_e^2}\left(-D_e \frac{\partial n_e}{\partial x} - \mu_e n_e E_x\right) - \frac{\beta_e}{1+\beta_e^2}\left(-D_e \frac{\partial n_e}{\partial y} - \mu_e n_e E_y\right) \qquad (7)$$

$$\Gamma_{e,y} = \frac{1}{1+\beta_e^2}\left(-D_e \frac{\partial n_e}{\partial y} - \mu_e n_e E_y\right) + \frac{\beta_e}{1+\beta_e^2}\left(-D_e \frac{\partial n_e}{\partial x} - \mu_e n_e E_x\right) \qquad (8)$$

$$|\Gamma_e| = \sqrt{\Gamma_{e,x}^2 + \Gamma_{e,y}^2} \qquad (9)$$

In Eqs. (5-8), β_e and β_+ are the electron and ion Hall parameters, μ_e and μ_+ are the mobilities, and D_e and D_+ are the diffusion coefficients [32],

52

$$\beta_+ = \mu_+ B_z, \quad \beta_e = \mu_e B_z \qquad (10)$$

$$D_+ = \mu_+ \frac{k_B T}{e}, \quad D_e = \mu_e \frac{k_B T_e}{e} \qquad (11)$$

The electron and ion mobilities, as well as the Townsend ionization coefficient in nitrogen are taken from Ref. [30,31],

$$\mu_+ = \frac{1.45 \times 10^3}{p^*} \frac{cm^2}{V \cdot s}, \quad \mu_e = \frac{4.4 \times 10^5}{p^*} \frac{cm^2}{V \cdot s}, \quad p^* = p(torr)\frac{300}{T}, \qquad (12)$$

$$\alpha = \begin{cases} 900 p^* \left(E/p^*\right)^{-1} \exp\left(-313 p^*/E\right), & E/p^* < 100 \ V/(cm \cdot torr) \\ 12 p^* \exp\left(-342 p^*/E\right), & E/p^* \geq 100 \ V/(cm \cdot torr) \end{cases} . \qquad (13)$$

To model the experimental conditions in M=3 nitrogen flows [11,12], in the present calculations the discharge pressure and temperature are P=7 torr and T=110 K. The electron temperature between the pulses is assumed to be T_e=1 eV. Note that the effective rate of electron-ion recombination in nitrogen plasmas is known with a significant uncertainty, because of the difference between the recombination rates of N_2^+ ions, β_{ei}=4.8·10^{-7}·$(300/T_e)^{1/2}$ cm^{3}s^{-1} N_4^+ ions, β_{ei}=2.0·10^{-6}·$(300/T_e)^{1/2}$ cm^{3}s^{-1} [33]. In the present model, which considers a single positive ion species, the recombination rate was chosen to provide the best agreement between the experimental and the calculated current decay rate between the ionizing high-voltage pulses, β_{ei}=1.4·10^{-7} cm^{3}s^{-1}.

The pulsed electric field, $E_p(t)$, used for calculations of the Townsend ionization coefficient in the repetitively pulsed discharge is evaluated as follows,

$$E_p(t) = \frac{U_p}{w} \exp\left[-\left(\frac{\sin[\pi v(t-t_0)]}{\sqrt{2}\,\tau}\right)^2\right], \qquad (14)$$

where U_p is the peak pulse voltage, w=2.4 cm is distance between the pulsed electrodes (2 cm test section depth plus the combined thickness of ceramic plates covering the pulsed electrodes in the experiments [11,12]), v=40 kHz is the pulse repetition rate, and $\tau=2.2 \cdot 10^{-3}$ is the non-dimensional pulse width parameter corresponding to the pulse full width at half maximum (FWHM) of 30 ns, as measured in the experiment [11,12]. The pulsed electric field is assumed to be uniformly distributed across a 4.5 cm x 3.0 cm rectangular domain shown in Fig. 1. Outside this region, the pulsed electric field is exponentially decreasing, by a factor of $1/e^2$ over a distance of 1 cm (both in the x and the y directions). The results of calculations using the present model, discussed in Section 3, were found to be sensitive to the pulsed electric field distribution on the periphery of the ionization region near the DC electrodes. Specifically, sudden fall-off of the pulsed electric field on the edges of the ionization region results in a higher predicted cathode voltage fall and a steeper current rise as the DC voltage is increased. Therefore the distance over which the pulsed field falls off was chosen to match the slope of the experimental current-voltage characteristic of the sustainer discharge in the absence of magnetic field.

The present model does take into account the pulsed electric field distribution in the z-direction (see Fig. 1), which can be strongly non-uniform. In particular, the model does not reproduce a significant voltage drop in the sheath regions formed near the pulsed electrodes, which could reach ~80-90% of the nanosecond pulse voltage between the electrodes [22]. Because of this, the pulsed electric field in the plasma is known with a significant uncertainty. Incorporating the pulsed electrode sheaths would require developing of a time-accurate, three-dimensional model of a repetitively pulsed nanosecond discharge in transverse DC sustainer electric field and transverse magnetic field. Since the duty cycle of the repetitively pulsed discharge is very low, ~1/1000 [11,12], development of such a model is an extremely challenging problem which would require massive computational resources. At this time, 3-D DC glow discharge models (e.g. see [34]) do not incorporate such extremely low duty cycle pulsed ionization processes. For this reason, in the present calculations the pulse voltage was an adjustable parameter, chosen to provide best agreement with the experimentally measured peak DC sustainer discharge current in the absence of magnetic field.

The boundary conditions on the cathode (at y=0), on the anode (at y=1), and away from the ionization region (at x=0 and x=1) are as follows:

$$y = 0 : \frac{\partial n_+}{\partial y} = 0, \; n_e = \gamma n_+ \frac{\mu_+}{\mu_e}, \; \varphi = 0 \tag{15}$$

$$y = 1 : n_+ = 0, \; \frac{\partial n_e}{\partial y} = 0, \; \varphi = 1 \tag{16}$$

$$x = 0, 1 : \frac{\partial n_+}{\partial x} = \frac{\partial n_e}{\partial x} = \frac{\partial \varphi}{\partial x} = 0 \tag{17}$$

The secondary electron emission coefficient from the cathode was taken to be $\gamma = 0.1$. The initial conditions assume uniform electron and ion concentrations throughout the ionization region ($n_e = n_i$) and linear electric potential distribution.

The model does not incorporate the external electrical circuit, and therefore the voltage on the DC electrodes is assumed to be constant. In the experiments, the DC voltage between the ionizing pulses actually somewhat varies, $U_{DC}(t) = U_{PS} - I(t) \cdot R$, where $U_{PS} = const$ is the power supply voltage, $I(t)$ is the current in the decaying plasma between the ionizing pulses, and R is the ballast resistor. The constant DC voltage was assumed to be equal to the time-averaged value of the experimental DC voltage between the pulses.

The system of partial differential equations (2-4) was solved by a stiff PDE integrator PDETWO [35] with a variable time step, using a central difference approximation for both the first and the second derivative terms. Maximum time step was set to 1 ns during the ionizing pulse and to 0.5 μs between the pulses. A nonuniform mesh (71 points in the x-direction and 351 points in the y-direction) was clustered near the edges of the pulsed ionization region in the x-direction and near the DC electrodes in the y-direction. No attempt was made to modify the integrator or the finite difference scheme to improve the numerical stability, which was controlled by limiting the time step and clustering the mesh. The system of equations was integrated until a periodic solution has been reached. Typically, this occurred after approximately 10 high voltage pulses. Convergence to a periodic solution was tested by comparing the electron density distributions and the sustainer current at $U_{DC} = 50$ V and $B = 0$, after 20 pulses (at 0.5 msec) and after 220 pulses (at 5.5 ms), which are close to each other. The time scale to obtain a

converged solution corresponds to a characteristic time for the ambipolar diffusion, ~1 ms at the present conditions.

As can be seen from Eqs. (5-8), in the present work the effect of transverse magnetic field on the drift-diffusion fluxes of the charged species is incorporated by taking into account the Hall effect. The Hall effect produces a component of the drift-diffusion fluxes in the direction perpendicular to both the electric and the magnetic field, i.e. in the ExB direction. In Eqs. (5-8), this is it taken into account by introducing the Hall parameters for the electrons and the ions, $\beta_e = \mu_e B$ and $\beta_+ = \mu_+ B$. Following this approximation, the electron and the ion flux vectors in the crossed E and B fields, Γ_e and Γ_+, are directed at Lorentz angles θ_e and θ_+ to the ExB vector, respectively, such as $\tan \theta_e = \beta_e$ and $\tan \theta_+ = \beta_+$. The validity and accuracy of this approximation has been discussed in greater detail in [36-38]. In Ref. [36], Monte Carlo simulation of a nitrogen plasma in crossed electric and magnetic fields was compared with the solution of the two-term Boltzmann equation in crossed fields [37]. The results showed that the components of the electron drift velocity (both in E and ExB directions), the Lorentz angle for the electrons, the mean electron energy, and the electron-neutral collision frequency are in satisfactory agreement with the predictions of a simple theory [38], as functions of the effective reduced electric field, $(E/N)_{eff} = (E/N)/(1 + \beta_e^2)^{1/2}$. This justifies the use of a drift-diffusion approximation in the present model.

3. Results and Discussion

3.1. B=0

Figure 3 compares the experimental [11] and the calculated current-voltage characteristics of the DC sustainer discharge in the absence of magnetic field. In Fig. 3, time-averaged experimental current and voltage are compared with the time-averaged current predicted by the model. It can be seen that the experimental results and the predictions of the model are in good agreement. Some disagreement between the model and the experiment is observed at low sustainer voltages, $U_{DC} < 300$ V (at I<0.12 A). In particular, the model predicts very low sustainer currents below $U_{DC} = 300$ V (I≈1 mA), while in the experiment the current starts rising at $U_{DC} \approx 200$ V and reaches I≈0.1 A at $U_{DC} = 300$ V. However, both the predicted cathode voltage fall (U_C, the x-intercept of the current voltage characteristic in Fig. 3) and the slope of the predicted current voltage curve at $U > U_C$ are close to the experimental values (see

56

Fig. 3). Figure 4, which compares the calculated time-dependent sustainer discharge current at $U_{DC}=500$ V with the experimental currents at $U_{DC}=480$ and 524 V, shows that the predicted rate of current decay between the pulses is close to the experiment. The current rise during the ionizing pulse is determined by the peak pulse voltage U_P (see Eq. (14)), while the current decay rate between the pulses is controlled by the electron-ion recombination coefficient, β_{ei}. The value of the peak pulse voltage used in the present calculation is $U_P=2.8$ kV, which is only about 20% of the pulse peak voltage of 13 kV [12] (see Fig. 2). This result is consistent with the 80-90% cathode voltage fall predicted by kinetic modeling of nanosecond pulse discharges [22].

Figure 5(a) shows a contour plot of period-averaged electron concentration at $U_{DC}=600$ V, normalized by the reference density of $n=2\cdot10^{11}$ cm^{-3}. One can see that the electron density is uniformly distributed across the ionization region. As can be seen from Fig. 5(b), showing the electron and the ion density distributions along the axis of symmetry of the discharge (at $X=0.5$), the ion density peaks near the cathode, as also occurs in the self-sustained DC discharge [31]. The space charge region near the cathode results in a stronger electric field (steeper potential gradient) in the cathode layer. Note that at the conditions of Fig. 5 ($U_{DC}=600$ V), the plasma in the bulk of the discharge volume is non-self-sustained (i.e. ionization in this region is produced only by the ionizing pulses). On the other hand, the cathode layer is self-sustained, with ionization produced mainly by the strong local DC field. The electron and the ion density distributions shown in Fig. 5(b) are also typical for a self-sustained DC glow discharge [31].

Figures 6 and 7 shows period-averaged electric potential and current density distributions at three different DC voltages, $U_{DC}=250$ V, $U_{DC}=400$ V, and $U_{DC}=600$ V. Potential distributions in Fig. 6 are normalized on the applied voltage, while the current density in Fig. 7 is shown in A/cm^2. In Figs. 6 and 7, contours are shown for every 10% of potential and current change (nine contours in each plot). One can see that at $U_{DC}=250$ V, DC electric field, i.e. the region of potential gradient, is confined to a narrow region near the cathode, so that the electric field does not penetrate into the plasma (see Fig. 6(a)). At these conditions, the applied voltage is too weak to generate ionization anywhere in the plasma, including the cathode layer, and it simply removes some of the electrons and the ions generated by the pulsed ionization. From Fig. 7(a), it can be seen that the current, with the peak current density of ~1 mA/cm^2, also runs around the ionized region without penetrating it. This type of truly non-self-sustained DC discharge is

known as Thomson discharge [39]. At this low applied voltage, the discharge current remains extremely low ($I \approx 0.8$ mA), as can be seen from Fig. 3.

As is well known, the cathode layer of a glow discharge becomes completely self-sustained when the overall rate of electron production in the cathode layer (both by electron impact ionization in the volume and by the secondary emission from the cathode) balances the rate of electron removal from the plasma by the applied field. This occurs when the Townsend self-sustaining criterion [15], $\alpha d = \ln(1 + 1/\gamma)$, where d is the cathode layer thickness, is satisfied. The applied voltage at which the cathode layer becomes self-sustained (i.e. the cathode voltage fall, U_C) can be determined from the x-intercept of the calculated current-voltage characteristic, $U_C \approx 300$ V, where the discharge current starts rising from near zero (see Fig. 3).

As the DC voltage increases, the electric field in the cathode region also increases until it exceeds the electric breakdown threshold and starts producing additional ionization by electron impact. This reduces charge separation in the cathode layer and results in deeper electric field penetration into the quasi-neutral region in the center of the plasma, where the equipotential lines become more equally spaced (see Fig. 6(b,c)). The field penetration into the plasma dramatically increases the current density, from less than 1 mA/cm^2 to a few tens of mA/cm^2 (see Fig. 7(b,c)). As can be seen, at $U>U_C$ the current distribution far from the cathode is rather uniform, while near the cathode it reaches maximum on the edges of the ionization region. This occurs because of the stronger charge separation in these regions and as a result, stronger electric field, which also has a horizontal (x) component (see Fig. 6 (b,c)). This effect is somewhat reduced at higher voltages (see Fig. 7(c)), when the current density distribution across the face of the cathode becomes more uniform.

Above the cathode voltage fall, at $U>U_C$, the discharge current increases approximately linearly (see Fig. 3). This shows that the plasma follows the Ohm's law, i.e. the plasma conductivity and the electron density both remain nearly constant. This occurs because the applied DC field does not produce any additional ionization in the bulk of the plasma (outside the cathode layer), so the discharge remains non-self-sustained.

3.2. B≠0

Figure 8 compares experimental and calculated current-voltage characteristics at the magnetic field of B=0.75 T, which corresponds to the electron Hall parameter of β_e=1.73,

showing good agreement. From Fig. 8, it can be seen that at B=0.75 T the sustainer discharge current is significantly lower than the current at the same sustainer voltage in the absence of magnetic field. This trend is detected both in the experiments [11] and in the present modeling calculations. This behavior is due to the Hall effect, which creates a current component in the **ExB** direction while reducing the current in the direction of the electric field (in the negative y-direction), and is described by the generalized Ohm's law [40],

$$ j_y = \frac{\sigma}{1+\beta_e^2} E_y \quad , \quad j_x = \beta_e \frac{\sigma}{1+\beta_e^2} E_y \quad . \tag{18} $$

In Eqs. (18), $\sigma = e n_e \mu_e$ is the scalar electric conductivity. Figure 9 compares the calculated time-dependent sustainer current at U_{DC}=700 V with the experimental currents at <U>=694 V and 726 V. As can be seen, the model somewhat underpredicts both the experimental current values and the rate of current decay between the ionizing pulses. However, the overall agreement between the model and the experiment is quite satisfactory.

From Fig. 8, one can see that in the presence of magnetic field, similar to the results at B=0, the sustainer current at low voltages (at $U<U_C \approx 300$ V) is very low, of the order of 1 mA. As discussed in Section 3.1, this occurs because the applied electric field does not penetrate into the plasma when the cathode layer is not self-sustained. To illustrate the effect of magnetic field on the plasma at these conditions, Fig. 10 shows contour plots of electric potential and current density, as well as the current vector at U_{DC}=50 V and B=1.5 T. From Fig. 10, it can be seen that at this low voltage the electric field remains confined to the region near the cathode, similar to the low-voltage case in the absence of magnetic field (see Fig. 6(a)). Again, the entire discharge, including the cathode layer, remains non-self-sustained. Both the electrons and the ions generated by the repetitively pulsed discharge diffuse out of the ionization region, which creates a weak ambipolar electric field due to the fact that the electrons diffuse faster than the ions. The outward motion of the electrons and the ions in this polarization field, in the presence of magnetic field directed out of the page, results in the counterclockwise electron drift (current) around the ionization region, in the **ExB** direction, as shown in Fig. 10 (b,c). Since the diffusion velocity of the ions is much lower, the resultant Lorentz force on the ions is also very low, and the ion drift (current) component in the **ExB** direction is negligibly small. Basically, the ions

simply diffuse in the outward direction, while the electron current circles around the ionized region. The peak current density is of the order of 1 mA/cm^2, while the total current predicted by the model at these conditions is I=0.2 mA. This is approximately two orders of magnitude lower than the value estimated from the Ohm's law at n_e=2·10^{11} cm^{-3} and σ=0.07 Si/m [11], I~A(j_x^2+j_y^2)$^{1/2}$ =25 mA. Here A=9 cm^2 is the effective cross sectional area of the DC electrodes (i.e. the length of the plasma in the x-direction times the depth of the test section in the z-direction, see Section 2).

This result provides insight into feasibility of MHD power generation in low-temperature supersonic flows with external ionization, such as a repetitively pulsed nanosecond discharge or an e-beam. In a typical laboratory scale, low-temperature, steady-state MHD experiment, the flow stagnation temperature is T_0=300 K, the Mach number, the magnetic field, and the flow velocity in the test section are M=3-4, B=1-2 T, and u=600-700 m/sec, respectively, and the MHD test section width is L~4-5 cm [11-13]. At these conditions, the MHD open voltage (i.e. the upper bound voltage between the MHD electrodes in the power generation regime) is U_{open}=uBL~30-60 V, which is much lower than the cathode voltage fall, U_C=200-300 V (e.g. see Fig. 8). The result of Fig. 10 clearly demonstrates that at U_{open}<U_C, the MHD current would be about two orders of magnitude lower than at the conditions when the cathode layer is self-sustained (at the same plasma conductivity). This makes power generation at these conditions extremely inefficient and basically not feasible. Our previous experiments also showed that the cathode voltage fall increases with the magnetic field, from U_C=250-300 V at B=0 to U_C=500 V at U=1.5 T [11], which makes the problem even more serious at higher magnetic fields. This analysis explains very low DC current values, I≤1 mA, measured in MHD power generation experiments [13]. In these experiments, the MHD current did increase with the applied DC voltage, U_{DC}≤244 V, but the voltage remained too low to self-sustain the cathode layer at the magnetic field of B=5 T. In MHD flow control experiments [11,12], self-sustaining cathode layer was produced by increasing the DC voltage above the cathode voltage fall, up to U_{DC}=1500 V. However, at this high voltage the MHD discharge cannot operate in the power generation regime since the MHD loading parameter at these conditions, K=E_y/uB$_z$≈40, is K>1. To circumvent this fundamental limitation, the size of the MHD section and/or flow stagnation temperature in the MHD power generation experiments would have to be considerably increased, by at least an order of magnitude.

Figure 11 shows contour plots of period averaged electron concentration, space charge density, and electric potential, respectively, at the conditions when the cathode layer is self-sustained (U_{DC}=700 V, B=0.75 T). Comparing Fig. 5 and Fig. 11, it can be seen that for the electric field and magnetic field configuration shown in Fig. 1 (**E** down, **B** out of the page), both the electrons and the ions are pushed to the left by Lorentz force. Since Lorentz force on the electrons is much greater due to the higher electron mobility, this creates negative space charge on the left side of the ionization region (see Fig. 11(b), where the low potential region penetrates further toward the anode, as shown in Fig. 11(c). At the same time, a positive space charge is formed on the right side of the ionization region, where the high potential regions extends closer to the cathode.

Figure 12 shows contour plot of the period-averaged current density, as well as the current and the electric field vectors at the conditions of Fig. 11. As can be seen, the current density is highest near the cathode and the anode, in particular near the upper left and lower right corners of the ionization region (see Fig. 12(a)). The current tilting angle with respect to the y-direction, caused by the Hall effect, is large close to the cathode and to the anode, where both the local electric field and the Lorentz force are strong, and low in the middle of ionization region, where the electric field is weaker (see Fig 12(b)). The x-component of the electric field vector near conducting surfaces (electrodes) is low, as shown in Fig. 12(c), where the electric field vectors are shown in the range of 0.1≤Y≤0.96. Basically, the current runs along an S-shaped curve, with the highest current density and the highest current tilting angle near the ends of an S. This behavior is consistent with experimental observations [41]. Figure 13 shows a photograph of a self-sustained pulsed DC discharge between two plane walls diverging at $1q^0$ each in quiescent room temperature air at P=5 torr, in the presence of transverse magnetic field of B=0.7 T directed out of the page. The pulse duration is 3 μsec, the peak voltage is U_{DC}=12.5 kV, and the distance between electrodes L=10 cm. From Fig. 13, one can see that the current indeed runs in an S-shaped pattern, qualitatively similar to the prediction of the present model. The difference between the predicted and the experimental current patterns can be seen near the ends of the S and is due to the fact that the present model assumes infinite continuous DC electrodes, while in the experiment [41] the discharge was produced between two small-size arrays of pin electrodes, visible near the top and the bottom walls in Fig. 13. Basically, in the present model the locations of the regions where the discharge is attached to the DC electrodes can vary, while

in the experiment [41] they remain fixed. In Fig. 12, the angle between the current density vector, j, and the electric field vector, E, is approximately 60° in the entire discharge region, which is consistent with the Lorentz angle for the electron Hall parameter of $\beta_e=1.73$, $\theta = \tan^{-1}\beta$ = 60°. Basically, the electric current runs at near Lorentz angle to the local electric field vector.

Charge separation in the x-direction because of the difference between the ion and the electron mobilities during their drift in the ExB direction (negative x-direction) caused by Lorentz force (see Fig. 11(b)) produces the polarization (Hall) electric field in the x-direction (see Fig. 12(c)). The polarization field accelerates the massive, slowly moving ions while slowing down the electron drift. As a result, between the ionizing pulses the entire plasma (i.e. the electrons and the ions together) is moving in the ExB direction with the ion slip velocity u_p [42]

$$u_p \approx \mu_e \mu_i E_y B_z \quad . \tag{19}$$

Plasma velocity in the negative x-direction between the pulses was evaluated at six different locations in the space charge region at the edges of ionization region, at Y= 0.8, 0.5, and 0.2, as shown in Fig. 14. This was done at the condition of Figs. 11, 12, at $U_{DC}=700$ V at B=0.75 T.

Figure 15(a) shows the normalized space charge density midway between the electrodes (at Y=0.5) at two different moments of time, t=0.1 μs and t=25 μs (i.e. right after the ionizing pulse and right before the next pulse). The period-averaged plasma velocity was estimated from the displacement of the peak charge density locations, $u_p(L2)=100$ m/sec and $u_p(R2)=50$ m/sec. Figure 15(b) also shows time-dependent ion slip velocities at these two locations, calculated from Eq. (19), using local time-dependent electric field values. It can be seen that the plasma velocities determined by these two methods are consistent. At four other locations, the period-averaged plasma velocities determined from the peak space charge shift are as follows: $u_p(L1)=190$ m/sec, $u_p(R1)=60$ m/sec, $u_p(L3)=70$ m/sec, and $u_p(R3)=100$ m/sec. The arrows shown in Fig. 14, which are proportional to the local plasma velocities, show the general trend of plasma displacement and distortion between the pulses. From Fig. 11(b) and Fig. 14, it can be seen that the charge density and the plasma velocity peak at the upper left and at the lower right corners of the ionization region (i.e. at L1 and R3 locations).

The estimated space charge propagation velocity is in satisfactory agreement with the prediction of Eq. (19), except at the location R3, where the electric field strongly depends on time. This illustrates the limit of applicability of the steady-state ion slip theory and of Eq. (19), which breaks down at the unsteady conditions. Equation (19) assumes that the Coulomb force on the electrons and on the ions are balanced, and that both groups are moving in the *ExB* direction at the same ion slip velocity, constant in time. Note that since the characteristic plasma decay time is 25-50 μsec (see Figs. 4,9), and since each ionizing pulse generates the plasma at the same location, the time-averaged displacement of the plasma does not exceed ~2.5-5 mm. This behavior is completely different from the behavior of a self-sustained DC discharge with long continuous electrodes in transverse magnetic field. In this case, the discharge filament moves in the *ExB* direction at a constant velocity of u_p relative to the flow ($u_p \pm u$ relative to the observer) [14].

Momentum transfer from the ions and the electrons in the plasma to the neutral flow, which is not included in the present discharge model, can be estimated as follows. The number of momentum transfer collisions per neutral particle is $N_{coll} \sim v_{coll} \tau_{res} n_e / N$, where v_{coll} is the elastic collision frequency between the charged species and the neutral species, $\tau_{res} = u/L$ is the flow residence time in the MHD discharge section, u is the baseline flow velocity, L is the length of the ionized region, and n_e is the plasma density. The neutral velocity change per collision is $\Delta u_{coll} \sim \delta \cdot u_{dr,x}$, where $u_{dr,x} = \mu E_x$ is the x-component of the charged particle drift velocity and δ is the fraction of charged particle momentum transferred per collision, $\delta \sim 2m_e/M_{N2}$ for electrons and $\delta \sim 1$ for ions. The resultant net neutral species velocity change in the MHD section is

$$\Delta u \sim N_{coll} \cdot \Delta u_{coll} \sim v_{coll} \tau_{res} \frac{n_e}{N} \cdot \delta u_{dr} \tag{20}$$

The neutral velocity change in the crossed pulser-sustainer discharge was estimated by averaging Δu predicted by Eq. (20) over the range of 0.35<X<0.65 and 0.2<Y<0.8 for the conditions of Figs. 11 and 12 (B=0.75 T, U_{DC}=700 V), using the period averaged x-components of ion and electron drift velocities predicted by the present model. For this estimate, we used the experimental flow conditions of Ref. [12], baseline flow velocity of u=620 m/sec, p=7 torr, and T=110 K (M=2.9). The estimated period-averaged neutral velocity change at these conditions is

$\Delta u \approx 0.7$ m/sec, with the contributions from the ions and from the electrons of ≈ 0.4 m/s and ≈ 0.3 m/s, respectively. This result is consistent with the prediction of a phenomenological quasi-one-dimensional MHD flow model [12] for the same conditions,

$$\Delta u = \frac{uLj_y B_z}{p(M^2 - 1)} = 1.1 \ m/s \ \ .$$

(21)

In Eq. (21), $j_y = 40$ mA/cm^2 is the average current density. This shows that both the microscopic and the macroscopic phenomenological models predict similar results for the neutral flow entrainment by the plasma. Note that the quasi-one-dimensional MHD model is also consistent with the experimental results on MHD flow deceleration [12]. Specifically, the model predicts $\Delta u = \pm 5.9$ m/s at $B = \pm 1.5$ T, $U_{DC} = 1500$ V, and $I = 1.0$ A ($j_y = 110$ mA/cm^2), which is close to the MHD-induced flow velocity difference inferred from the static pressure measurements in M=3 nitrogen and dry air flows at these conditions,

$$\Delta u_{\pm} = \Delta u_+ - \Delta u_- = \frac{u}{(\gamma - 1)M^2 + 1} \cdot \frac{\Delta p_+ - \Delta p_-}{p} \ \ ,$$

(22)

$\Delta u_{\pm} = 13$ m/sec [12]. In these measurements, the relative static pressure change due to MHD interaction was $(\Delta p_+ - \Delta p_-)/p \approx 0.10$, which shows that supersonic flow velocity change of only about 2%, at a low MHD interaction parameter $\eta \sim 0.01$, is detectable. Consistency between the two models and the experimental results also demonstrates that incorporating momentum transfer to the neutrals in charge-neutral collisions into the present two-dimensional discharge model would allow accurate prediction of the neutral flow entrainment by the MHD plasma.

4. Summary

Kinetic modeling of the crossed pulser-sustainer discharge in the presence of transverse magnetic field is used to obtain insight into kinetics of a low-temperature MHD plasma in nitrogen. Uniform ionization in the discharge is produced by repetitive high voltage, nanosecond duration pulses, while the DC sustainer discharge couples power to the decaying plasma between

the pulses. Previously, this discharge has been used for MHD control of density fluctuations in supersonic boundary layer, low-temperature supersonic air flow deceleration, and demonstration of MHD plasma generation in cold unseeded air flows. The model predictions are compared with the experimental sustainer discharge current-voltage characteristics and time-dependent current traces, both in the absence and presence of magnetic field, showing satisfactory agreement. In the absence of magnetic field, the calculations show that at low DC voltages, $U_{DC}<300$ V, the entire discharge, including the cathode layer, remain non-self-sustained, which results in very low sustainer discharge current. At higher voltages, when the cathode layer becomes self-sustained, the sustainer current grows approximately linearly with the DC voltage, which shows that the plasma conductivity remains nearly constant. This occurs because the applied DC field does not produce any additional ionization in the bulk of the plasma (outside the cathode layer), so the discharge remains non-self-sustained. As the voltage increases, the current density in the self-sustained cathode layer becomes more uniform.

In the presence of magnetic field, the sustainer current is significantly lower than the current at the same sustainer voltage in the absence of magnetic field, due to the Hall effect. At low DC voltages (below the cathode voltage fall, $U_C \approx 300$ V), electric field does not penetrate into the plasma, while the sustainer current remains very low (two orders of magnitude below the Ohm's law prediction) and circles around the pulsed ionization region. This demonstrates that MHD power generation in low-temperature plasmas with open MHD voltages below the cathode fall is not feasible. At high DC voltages ($U_{DC}>U_C$), when the cathode layer becomes self-sustained, the model predicts significant electron and ion drift in the **ExB** direction due to Lorentz force, while the current runs in an S-shape pattern due to the Hall effect. Charge separation induced by the disparity between the electron and ion mobilities also causes the entire plasma to shift in the in the **ExB** direction approximately at the ion slip velocity.

Estimated neutral flow velocity change due to collisional momentum transfer from the charged species to the neutral species is consistent with the prediction of the quasi-one-dimensional phenomenological MHD flow equations, as well as with previous experimental results. This demonstrates that incorporating momentum transfer in charge-neutral collisions into the present two-dimensional repetitively pulsed discharge model would allow accurate prediction of the neutral flow entrainment by the low-temperature MHD plasma.

References

1. I.V. Adamovich, J.W. Rich, and G.L. Nelson, "Feasibility Study of Magneto-hydrodynamics Acceleration of Unseeded and Seeded Air Flows," AIAA Journal, Vol. 36, No. 4, 1998, pp. 590-597

2. V.L. Fraishtadt, A.L. Kuranov, and E.G. Sheikin, "Use of MHD Systems in Hypersonic Aircraft," Technical Physics, Vol. 43, No. 11, 1998, pp. 1309-1314

3. C. Park, U.B. Mehta, and D. W. Bogdanoff, "Magnetohydrodynamic Energy Bypass Scramjet Performance with Real Gas Effects," Journal of Propulsion and Power, Vol. 17, No. 5, 2001, pp. 1049-1057

4. S.O. Macheret, M.N. Shneider, R.B. Miles, and R.J. Lipinski, "Electron Beam Generated Plasmas in Hypersonic MHD Channels," AIAA Journal, Vol. 39, No.6, 2001, pp. 1127-1136

5. S.O. Macheret, M.N. Shneider, R.B. Miles, "Magnetohydrodynamic Control of Hypersonic Flow and Scramjet Inlets Using Electron Beam Ionization," AIAA Journal, Vol. 40, No.1, 2002, pp. 74-81

6. S.O. Macheret, M.N. Shneider, R.B. Miles, "MHD Power Extraction from Cold Hypersonic Air Flow with External Ionizers," Journal of Propulsion and Power, Vol. 18, No. 2, 2002, pp. 424-431

7. A.L. Kuranov and E.G. Sheikin, "Magnetohydrodynamic Control on Hypersonic Aircraft Under "Ajax" Concept," Journal of Spacecraft and Rockets, Vol. 40, No. 2, 2003, pp. 174-182

8. S.V. Bobashev, Yu.P. Golovachov, and D.M. Van Wie, "Deceleration of Supersonic Plasma Flow by an Applied Magnetic Field," Journal of Propulsion and Power, 2003, Vol.19, No. 4, pp. 538-546

9. J. S. Shang, R. Kimmel, J. Hayes, C. Tyler and J. Menart, "Hypersonic Experimental Facility for Magnetoaerodynamic Interactions", Journal of Spacecraft and Rockets, vol. 42, No. 5, 2005, pp. 780-789

10. R. Meyer, M. Nishihara, A. Hicks, N. Chintala, M. Cundy, W.R. Lempert, I.V. Adamovich, and S. Gogineni, "Measurements of Flow Conductivity and Density Fluctuations in Supersonic Nonequilibrium MHD Flows," AIAA Journal, Vol. 43, No. 9, 2005, pp. 1923-1930

11. M. Nishihara, N. Jiang, J.W. Rich, W.R. Lempert, I.V. Adamovich, and S. Gogineni. "Low-Temperature Supersonic Boundary Layer Control Using Repetitively Pulsed MHD Forcing," Physics of Fluids, Vol. 17, 2005, pp. 106102-106102-12

12. M. Nishihara, J.W. Rich, W.R. Lempert, I.V. Adamovich, and S. Gogineni. "Low-Temperature M=3 Flow Deceleration by Lorentz Force," Physics of Fluids, Vol. 18, 2006, pp. 086101-086101-11

13. R.C. Murray, S.H. Zaidi, M.R. Carraro, L.M. Vasilyak, S.O. Macheret, M.N. Shneider, and R.B. Miles, "Magnetohydrodynamic Power Generation Using Externally Ionized, Cold, Supersonic Air as Working Fluid", AIAA Journal, vol. 44, No. 1, 2006, pp. 119-127

14. S. Zaidi, T. Smith, S. Macheret, and R. Miles, "Snowplow Surface Discharge in Magnetic Field for High Speed Boundary Layer Control", AIAA Paper 2006-1006, 44th AIAA Aerospace Sciences Meeting and Exhibit, Reno, Nevada, Jan. 9-12, 2006

15. Yu.P. Raizer, "Gas Discharge Physics," Springer-Verlag, Berlin, 1991

16. A. E. Hill, "Continuous Uniform Excitation of Medium-Pressure CO_2 Laser Plasmas by Means of Controlled Avalanche Ionization", Appl. Phys. Lett., Vol. 22, No. 12, 1973. p. 670

17. N.A. Generalov, V.P. Zimakov, V.D. Kosynkin, Yu.P, Raizer, and D.I. Roitenburg, "Method for Significantly Increasing the Stability Limit of the Discharge in Fast-Flow Large-Volume Lasers", Technical Physics Letters, Vol. 1, No. 5, 1975, p. 201

18. N.G. Basov, I.K, Babaev, V.A. Danilychev, M.D. Mikhailov, V.K. Orlov, V.V. Savelev, V.G. Son, and N.V. Cheburkin, "Closed Cycle CW CO_2 Laser Employing an Electron Beam Ionizer", Soviet Journal of Quantum Electronics, vol. 6, No. 4, 1979, pp. 772-781

19. A.S. Kovalev, E.A. Muratov, A.A. Ozerenko, A.T. Rakhimov, and N.V. Suetin, "Structure of a Beam-Driven RF Discharge in a Gas Flow", Soviet Journal of Plasma Physics, vol. 11, 1985, No. 7, pp. 515-519

20. A.P. Napartovich, "Physics of High-Power CO Laser", in "Gas Lasers - Recent Developments and Future Prospects", W.J. Witteman, V.N. Ochkin (eds.), NATO ASI Series, 1996, pp. 11–22

21. S.O. Macheret, M.N. Shneider, and R.B. Miles, "Modeling of Air Plasma Generation by Repetitive High-Voltage Nanosecond Pulses", IEEE Transactions on Plasma Science, vol. 30, No. 3, 2002, pp. 1301-1314

22. S.O. Macheret, M.N. Shneider, and R.C. Murray, "Ionization in strong electric fields and dynamics of nanosecond-pulse plasmas", Physics of Plasmas, vol. 13, 2006, pp. 023502-023502-10

23. C.H. Kruger, C.O. Laux, L. Yu, D.M. Packan, and L. Pierrot, "Nonequilibrium Discharges in Air and Nitrogen Plasmas at Atmospheric Pressure," Journal of Pure and Applied Chemistry, vol. 74, No. 3, 2002, pp. 337-347

24. S.A. Bozhenkov, S.M. Starikovskaya, and A.Yu. Starikovskii, "Nanosecond Gas Discharge Ignition of H_2- and CH_4-containint mixtures", Combustion and Flame, vol. 133, 2003, pp. 133-146

25. S.M. Starikovskaia, E.N. Kukaev, A.Yu. Kuksin, M.M. Nudnova M M, and A.Yu. Starikovskii, "Analysis of the Spatial Uniformity of the Combustion of a Gaseous Mixture Initiated by a Nanosecond Discharge", Combustion and Flame, vol. 139, 2004, pp. 177–87

26. G. Lou, A. Bao, M. Nishihara, S. Keshav, Y.G. Utkin, J.W. Rich, W.R. Lempert, and I.V. Adamovich, "Ignition of Premixed Hydrocarbon-Air Flows by Repetitively Pulsed, Nanosecond Pulse Duration Plasma", Proceedings of the Combustion Institute, vol. 31, Issue 2, January 2007, pp. 3327-3334

27. A. Hicks, S. Norberg, P. Shawcross, W.R. Lempert, J.W. Rich, and I.V. Adamovich, "Singlet Oxygen Generation in a High Pressure Non-Self-Sustained Electric Discharge", Journal of Physics D: Applied Physics, vol. 38, 2005, pp. 3812-3824

28. A. Hicks, Yu.G. Utkin, W.R. Lempert, J.W. Rich, and I.V. Adamovich, "Continuous Wave Operation of a Non-Self-Sustained Electric Discharge Pumped Oxygen-Iodine Laser", Applied Physics Letters, vol. 89, 2006, p. 241131

29. A. Hicks, S. Tirupathi, N. Jiang, Yu. Utkin, W.R. Lempert, J.W. Rich, and I.V. Adamovich, "Design and Operation of a Supersonic Flow Cavity for a Non-Self-Sustained Electric Discharge Pumped Oxygen-Iodine Laser", accepted for publication in Journal of Physics D: Applied Physics, 2007

30. Yu.P. Raizer and S.T. Surzhikov, "Two-Dimensional Structure in a Normal Glow Discharge and Diffusion Effects in Cathode and Anode Spot Formation," High Temperature, Vol. 26, 1988, pp. 304-311

31. S.T. Surzhikov and J.S. Shang, "Two-Component Plasma Model for Two-Dimensional Glow Discharge in Magnetic Field," Journal of Computational Physics, Vol. 199, 2004, pp. 437-464

32. L.G. Huxley, R.W. Crompton, "The Drift and Diffusion of Electrons in Gases," Wiley, New York, 1974

33. J. Poggie, "DC Glow Discharges: A Computational Study for Flow Control Applications," AIAA Paper 2005-5303, 36th AIAA Plasmadynamics and Lasers Conference, Toronto, Canada, June 6-9, 2005

34. V. Guerra and J. Loureiro, "Electron and heavy particle kinetics in a low-pressure nitrogen glow discharge," Plasma Sources Science and Technology, Vol. 6, 1997, pp. 361-372

35. N.K. Madsen and R.F. Sincovec, "Algorithm 540: PDECOL, General Collocation Software for Partial Differential Equations [D3]," ACM Transactions on Mathematical Software, Vol. 5, 1979, p. 326

36. G.R.G. Raju and M.S. Dincer, "Monte Carlo Simulation of Electron Swarms in Nitrogen in Uniform ExB Fields," IEEE Transactions on Plasma Science, Vol. 18, No. 5, 1990, pp. 819-825

37. G.R.G. Raju and G.R. Gurumurthy, "Electron Energy Distributions and Transport Coefficients in N_2 in ExB Fields," International Journal of Electronics, Vol. 44, 1978, pp. 355-365

38. A.E.D. Heylen, "Electrical Ionization and Breakdown of Gases in a Crossed Magnetic Field," IEE Proceedings, Vol. 127, Pt. A, No. 4, 1980, pp. 221-244

39. I.V. Adamovich, "Control of Electron Recombination Rate and Electron Density in Optically Pumped Nonequilibrium Plasmas," Journal of Physics D: Applied Physics, Vol. 34, 2001, pp. 319-325

40. G. W. Sutton and A. Sherman, "Engineering Magnetohydrodynamics", McGraw-Hill, New York, 1965

41. A.V. Erofeev, T.A. Lapushkina, S.A. Poniaev, R.V. Vasil'eva, B.G. Zhukov, and S.V. Bobashev, "Influence of Magnetic Field on Gas Discharge Used for Air Ionization," AIAA Paper 2007-0434, 45th AIAA Aerospace Sciences Meeting and Exhibit, Reno, Nevada, Jan. 8-11, 2007

42. S.O. Macheret, "Physics of Magnetically Accelerated Nonequilibrium Surface Discharges in High-Speed Flow," AIAA Paper 2006-1005, 44th AIAA Aerospace Sciences Meeting and Exhibit, Reno, Nevada, Jan. 9-12, 2006
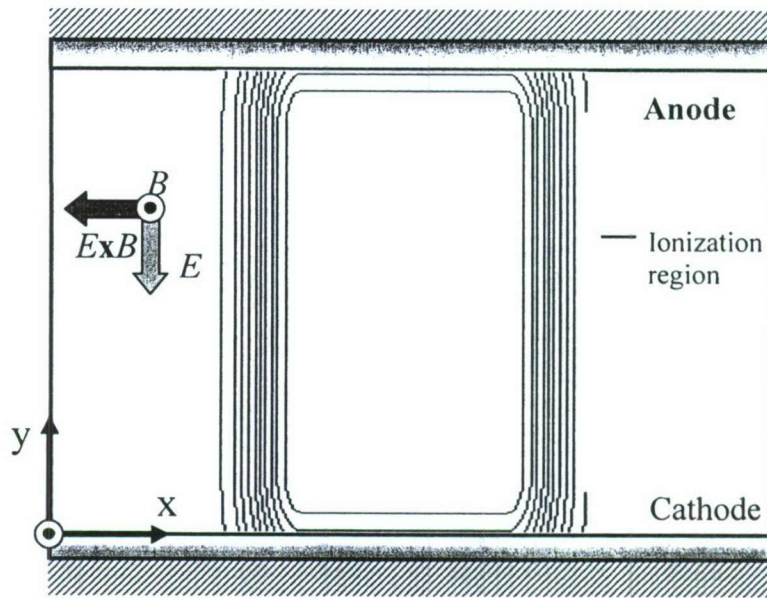
Figure 1. Schematic of the integration domain of the DC discharge sustained by the repetitive high voltage ionizing pulses in transverse magnetic field. The size of the integration domain is 9 cm in the x-direction by 4 cm in the y-direction. Pulsed electric field is parallel to magnetic field.
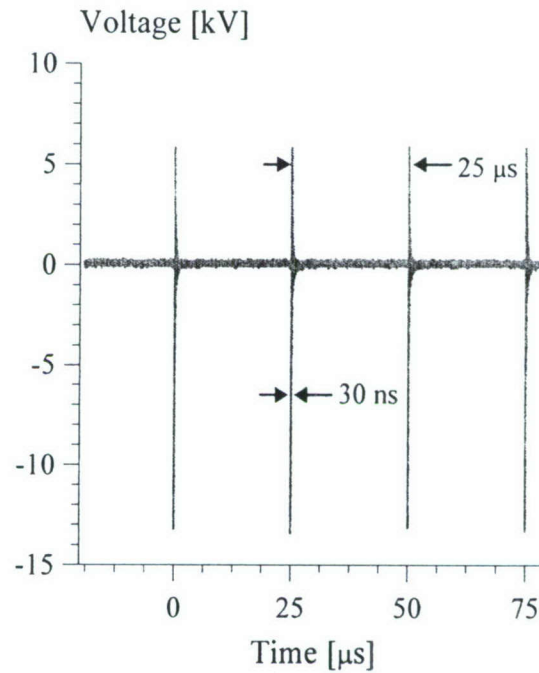
Figure 2. Typical repetitively pulsed voltage waveform. M=3 nitrogen flow at P_0=250 torr, P_{test}=8.4 torr, and B=1.5 T [12]. Pulse repetition rate is v=40 kHz.
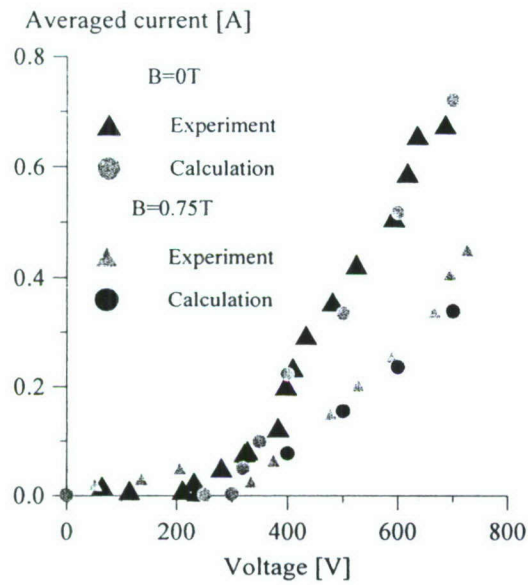
71
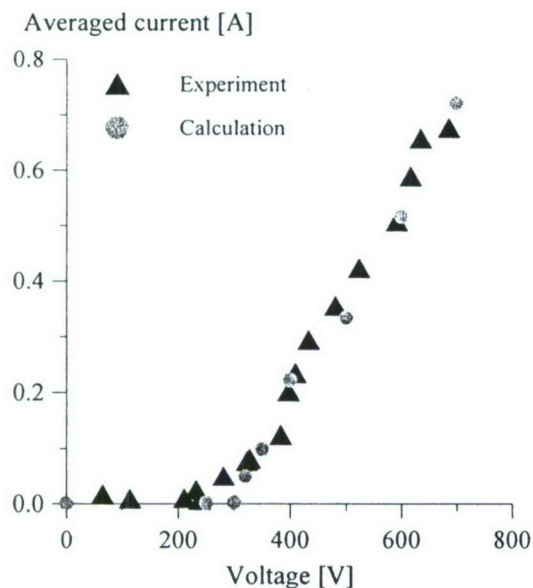
Figure 3. Time-averaged experimental [11] and calculated current voltage characteristics of the sustainer discharge at B=0, ν=40 kHz.
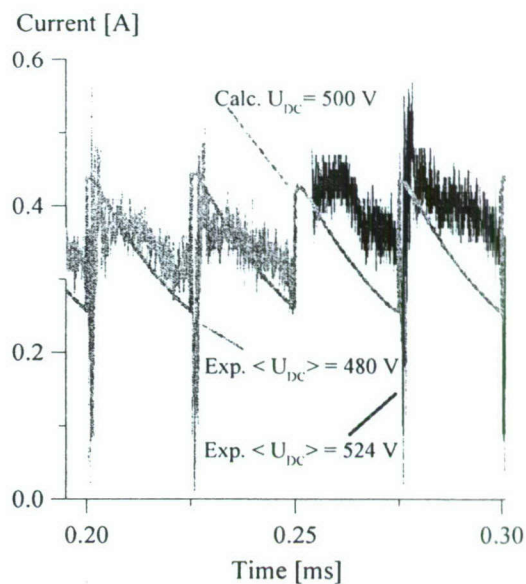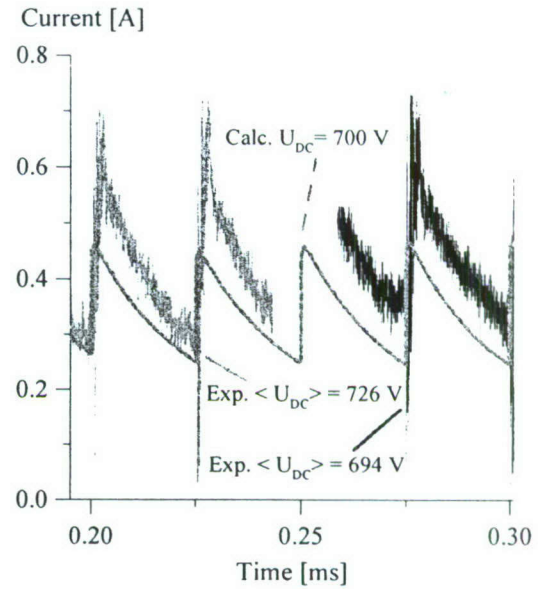

Figure 4. Time-resolved experimental sustainer discharge current at U_{DC}=480 and 524 V [11] and calculated current at U_{DC}=500 V. B=0, ν=40 kHz.


(a)

(b)
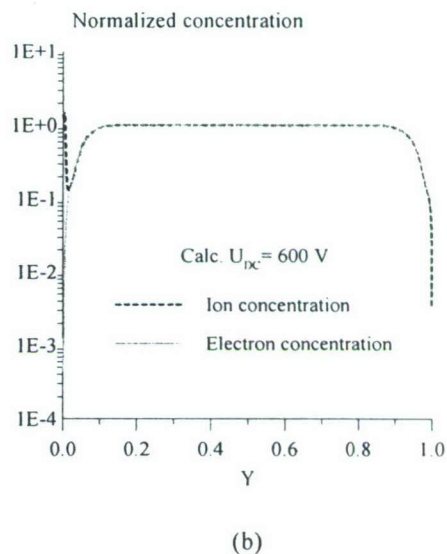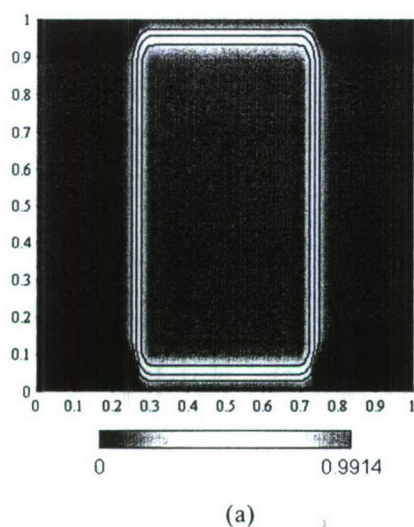
Figure 5. (a) Contour plot of period-averaged electron concentration and (b) period- averaged electron and ion concentration distributions along the line of symmetry (at X=0.5) at U_{DC}=600 V. B=0, ν=40 kHz, electron concentration is normalized on n=2·10^{11}cm^{-3}.
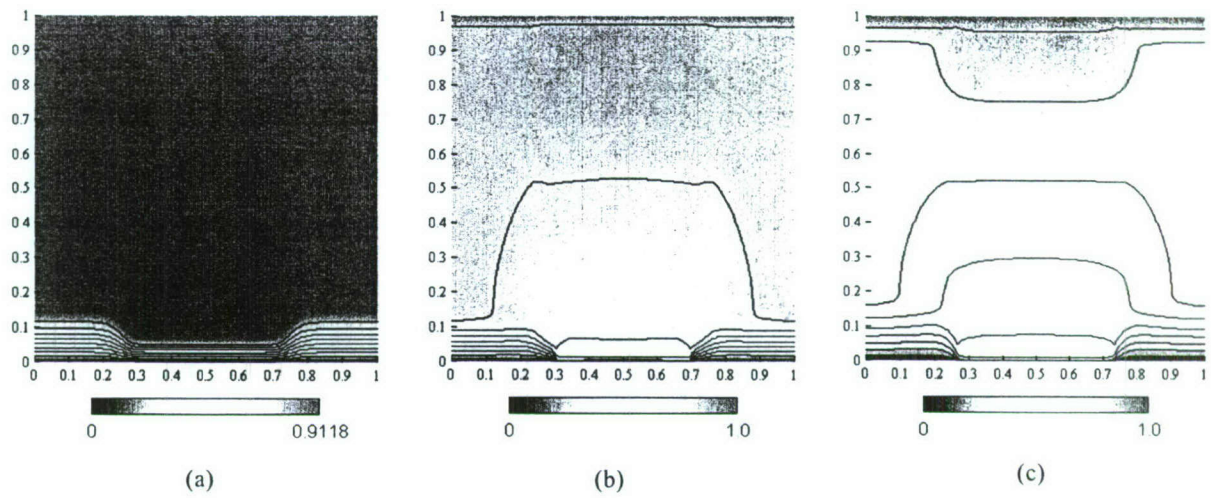
Figure 6. Period-averaged potential distributions at U_{DC}=250 V (a), 400 V (b), and 600 V (c). B=0, ν=40 kHz, the values on the contour plots are normalized on the applied DC voltage.
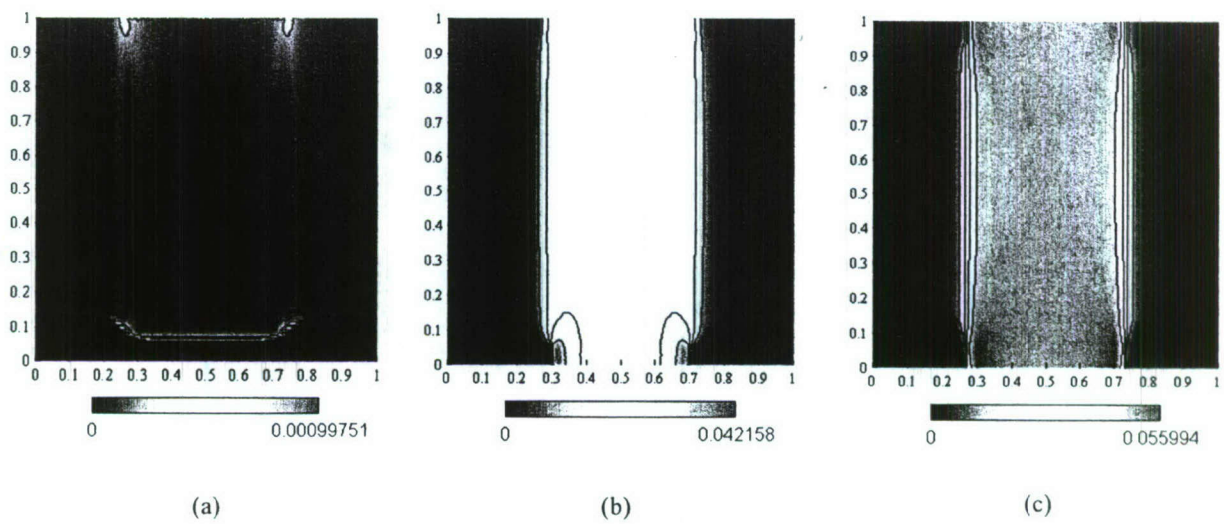
Figure 7. Period-averaged current distributions (in A/cm2) at U_{DC}=250 V (a), 400 V (b), and 600 V (c) at the conditions of Fig. 6.

Figure 8. Time-averaged experimental [11] and calculated current voltage characteristics of the sustainer discharge at B=0.75 T, ν=40 kHz.

Figure 9. Time-resolved experimental sustainer discharge current at U_{DC}=694 V and 726 V [11] and calculated current at U_{DC}=700 V. B=0.75 T, ν=40 kHz.

(a)

(b)

(c)
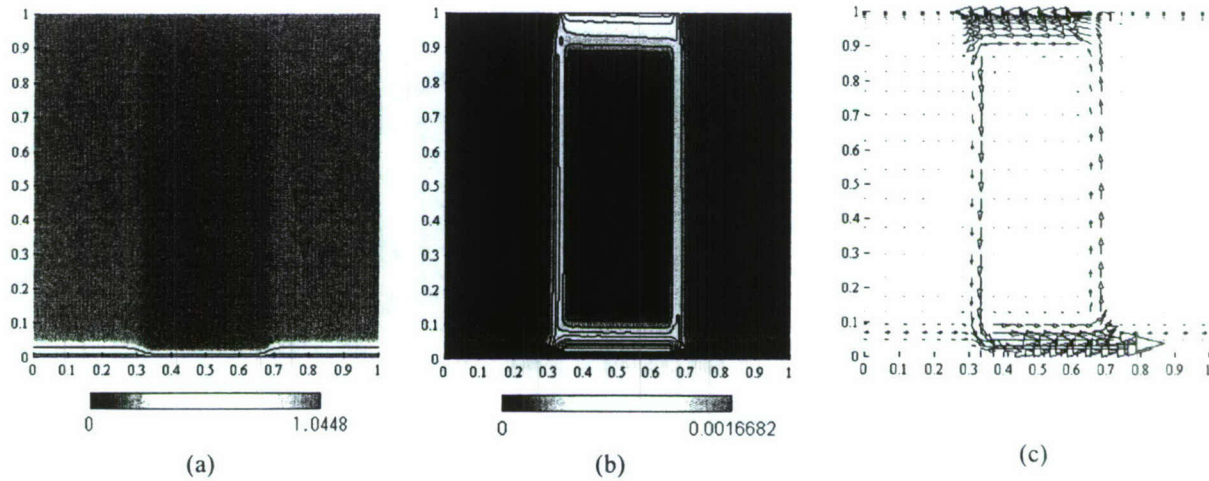
Figure 10. Period averaged potential distribution (a), current density distribution in A/cm^2 (b), and current vector field (c). U_{DC}=50 V, B=1.5 T, ν=40 kHz.

74
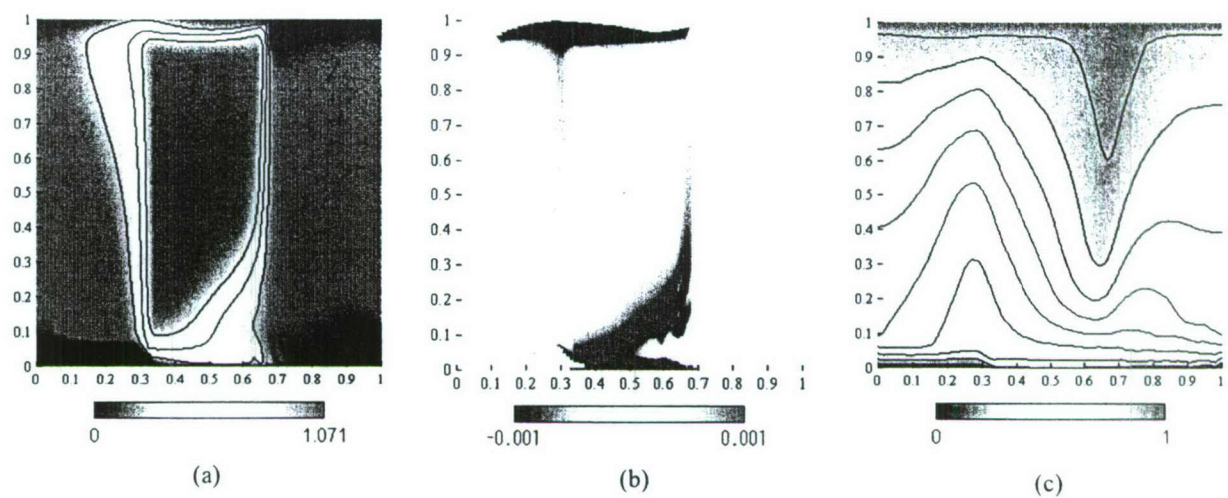
Figure 11. Period-averaged electron concentration distribution (a), space charge distribution (b), and potential distribution (c). U_{DC}=700 V, B=0.75 T, ν=40 kHz.
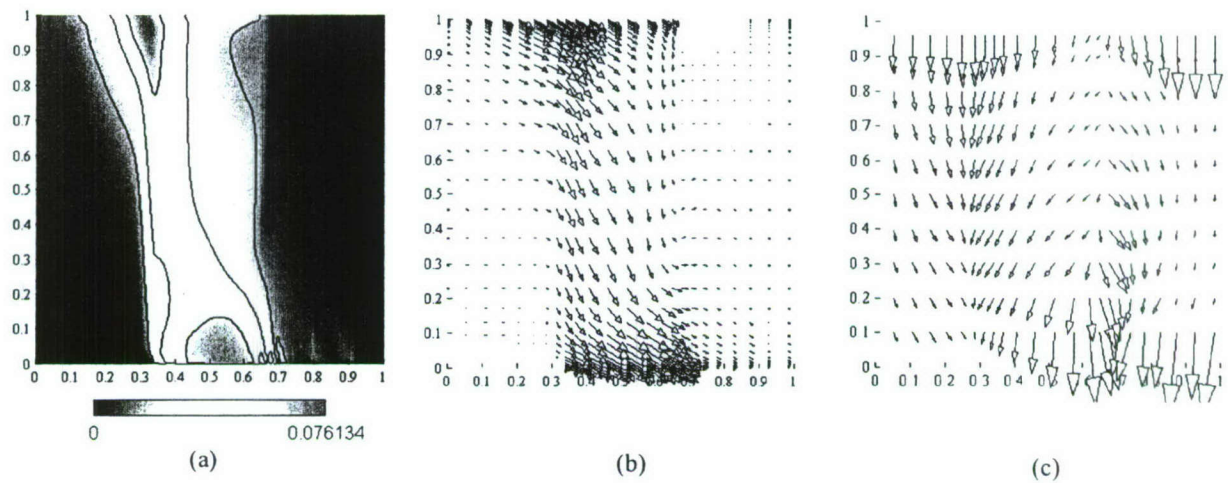

Figure 12. Period-averaged current density distribution in A/cm^2 (a), current vector (b), and electric field vector in the range of 0.1<Y<0.96 at the conditions of Fig. 11.
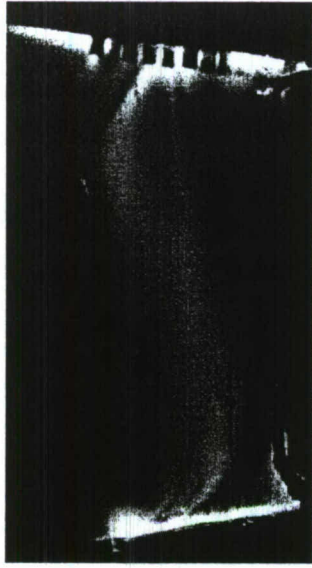
Figure 13. Photograph of transverse pulsed DC discharge in stagnant air at P=5 torr. Interelectrode distance 10 cm, U_{DC}=12.5 kV, B=0.7 T [39].
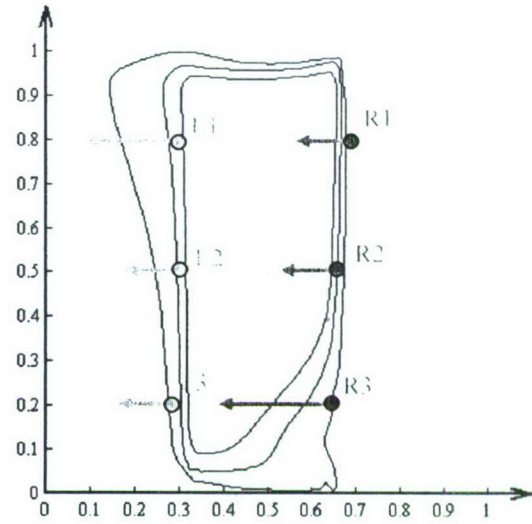

Figure 14. Six locations in the space charge region, shown in Fig. 11(b), where plasma propagation velocity was monitored.
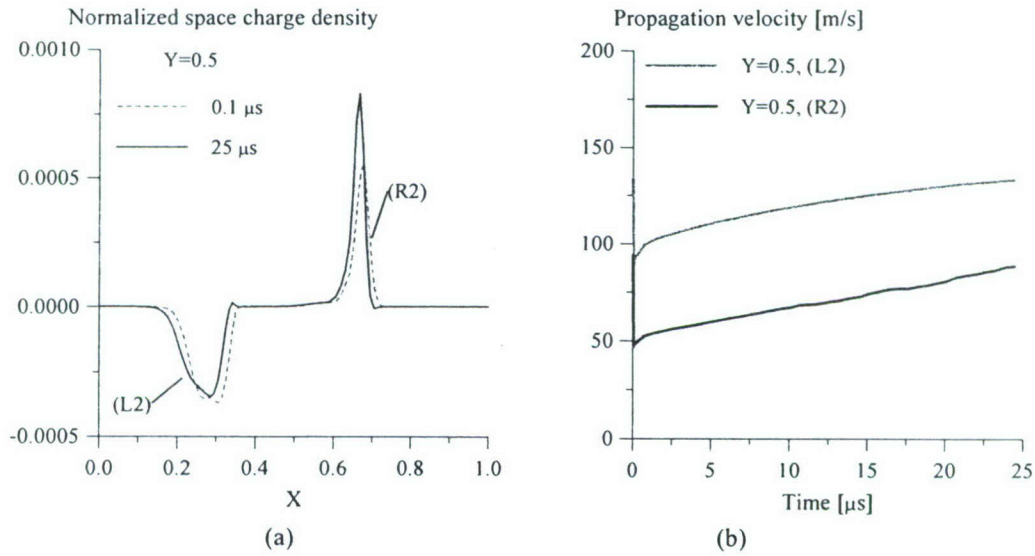

(a)

(b)

Figure 15. Instantaneous normalized space charge density at two different moments of time (a) and ion slip velocity predicted by Eq. (19) (b) at Y=0.5. Conditions are the same as in Figs. 11, 12.

76